POLITECNICO
MILANO 1863

SCUOLA DI INGEGNERIA INDUSTRIALE
E DELL'INFORMAZIONE

High speed electro-optical dual comb spectrometer in a single path configuration

Tesi di Laurea Magistrale in
Engineering Physics - Ingegneria Fisica

Author: **Luca Melesi**

Student ID: 103608
Advisor: Prof. Davide Gatti
Academic Year: 2023-24

Abstract

Multispecies gas detection based on laser spectroscopy has gained tremendous advances with the advent of frequency combs thanks to their spectral properties that allows to simultaneously probe thousand absorption lines of several molecules. Specifically, the dual comb approach enables the design of completely non-invasive, highly selective, sensitive and ultrafast chemical sensors that can found a plethora of applications in completely different field from breath analysis to atmospheric studies.
Real-time monitoring at microsecond rate is highly desirable to study chemical kinetics of combustion processes e.g., fuel pyrolysis, oxidation, heat release and pollutant formation. In this respect, dual-comb spectrometers based on electro-optic combs offer the highest acquisition speed among various implementations due to their relatively narrow bandwidth. Additionally, electro-optic (EO) combs enable the implementation of compact and portable spectrometers, making them ideal for field measurements.
This thesis aims at developing a portable spectrometer for simultaneous analysis of multiple chemicals. For the first time we combine a Single-Sideband Modulator (SSM) driven by an Arbitrary Waveform Generator (AWG) to synthesize in a single-path fully-fibered configuration a 25 GHz bandwidth dual-comb for high-speed absorption measurements.
The optimal method for generating EO combs with high throughput and high spectral flatness, as identified through simulations, involves a parabolic phase relationship between modes. A RF comb with these features was then synthesized using an AWG, and characterized demonstrating excellent agreement with the simulation results.
A prototypical electronic board was designed using EAGLE and implemented to interface with and manage the multiple voltage signals required to drive the SSM. All components underwent testing, ranging from the single-mode behavior of the laser to temperature stabilization and the bias current requirements for the internal semiconductor amplifiers. A software was realized in the LabView environment to provide the different voltages with the right timing. To ensure portability the overall system has been finally mounted on a home made modular cart with wheels and in the next future will be completely tested.

Keywords: Dual comb spectroscopy, Molecular spectroscopy, Chemical kinetics.

Abstract in lingua italiana

Il monitoraggio di miscele di gas basato sulla spettroscopia laser ha ottenuto enormi progressi con l'avvento dei pettini di frequenza, grazie alle loro proprietà spettrali che permettono di sondare simultaneamente migliaia di linee di assorbimento di diverse molecole. In particolare, l'approccio dual comb consente di progettare sensori chimici non invasivi, altamente selettivi, sensibili e veloci che possono trovare una miriade di applicazioni in campi completamente diversi, dall'analisi del respiro agli studi atmosferici.
In questo contesto, gli spettrometri a doppio pettine basati su pettini elettro-ottici offrono la massima velocità di acquisizione grazie alla loro banda relativamente stretta consentendo di realizzare spettrometri compatti e portatili, ideali per le misurazioni sul campo. Questa tesi si propone di sviluppare uno spettrometro portatile per l'analisi simultanea di più sostanze chimiche. Per la prima volta, un modulatore Single-Side Band (SSM) pilotato da un Generatore di Forma d'Onda Arbitraria (AWG) viene utilizzato per sintetizzare un pettine doppio con una larghezza di banda di 25 GHz per misurazioni di assorbimento spettrale ad alta velocità.
Il metodo ottimale per generare pettini elettro-ottici mantenendo uno spettro più uniforme possibile e massimizzando la potenza di uscita, individuato tramite simulazioni, prevede una relazione parabolica di fase tra i modi del pettine. Un pettine RF con queste caratteristiche è stato quindi sintetizzato utilizzando un AWG e caratterizzato, dimostrando un'eccellente concordanza con i risultati delle simulazioni.
È stata progettata e realizzata una scheda elettronica prototipale mediante EAGLE per gestire i segnali di tensione multipli necessari per pilotare l'SSM. Tutti i componenti sono stati testati, dall'andamento in singolo modo del laser alla stabilizzazione della temperatura, ai requisiti di corrente di polarizzazione per gli amplificatori a semiconduttore.
Un software è stato sviluppato in ambiente LabView per fornire le diverse tensioni con il giusto timing. Per garantire la portabilità, l'intero sistema è stato montato su un carrello modulare con ruote e sarà a breve completamente testato.

Parole chiave: Spettroscopia a doppio pettine, Spettroscopia molecolare, Cinetica chimica.

Contents

Abstract **i**

Abstract in lingua italiana **iii**

Contents **v**

Introduction **1**

1 Principles of Molecular Spectroscopy **3**

1.1 Light Matter Interaction 3

1.1.1 Density Matrix Approach for a Two-Level System 5

1.1.2 Spectral Line Intensity of Molecules 10

1.2 Line Broadening Mechanisms 12

1.2.1 Homogeneous Broadening Mechanisms 12

1.2.2 Inhomogeneous Broadening Mechanisms 15

1.2.3 Voigt Profile 16

1.3 Molecular Energy Levels and Transitions in the IR Region 17

1.3.1 Rotational Energy Levels 17

1.3.2 Vibrational and Rovibrational Energy Levels 20

2 Electro Optic Dual Comb Spectroscopy **23**

2.1 Optical Frequency Combs 23

2.2 Electro Optic Combs 27

2.2.1 Theory of E-O Combs 29

2.2.2 EOM 30

2.2.3 AOM 31

2.2.4 Single Sideband Modulator 32

2.3 Dual Comb Spectroscopy 35

2.3.1 DCS: The Ideal Case 38

2.3.2 DCS With Imperfect Combs 41
2.3.3 Dual Path EO-DCS 42
2.3.4 Single Path EO-DCS 44

3 Experimental Setup **47**
3.1 Spectrometer Layout 47
3.2 Low Noise Single Mode Laser 50
3.3 Arbitrary Waveform Generator 50
3.4 Single Sideband Modulator 52
3.4.1 MXPM90 Cable 53
3.4.2 Alpes Laser TC-3 53
3.4.3 WTC 32ND 54
3.4.4 PLD12.5K-CH 55
3.5 Board 56
3.5.1 TL974IN 58
3.6 PCIe 6738 58
3.6.1 LabView Code 58

4 Simulation and Testing **63**
4.1 Design and optimization of the EO-comb 63
4.2 AWG-based synthesis of a microwave dual-comb signal 65
4.3 Development and testing of an electronic interface board driving the SSM . 69

5 Conclusions **77**

Bibliography **79**

List of Figures **83**

Introduction

Laser absorption spectroscopy is an invaluable diagnostic tool for various chemical systems and practical applications that enable to design sensors that has the advantage to be non-invasive, highly selective, sensitive, accurate, and in some case portable.
Multi-species detection at high speeds has been challenging due to the lack of suitable laser sources. This capability is particularly crucial for studying transient reaction systems, such as fuel pyrolysis, oxidation, heat release, and pollutant formation. Optical frequency combs (OFCs) show promise in this area owing to their spectral structure, which consists of discrete, evenly spaced narrow modes capable of simultaneously probing multiple species. However, exploiting this capability requires detection systems that can effectively discriminate the various spectral contributions.
Among the techniques developed for this purpose, dual-comb spectroscopy (DCS) stands out. This makes DCS well-suited for observing ultrafast chemical kinetics in the gas phase. However, when combs are generated through mode-locked lasers, DCS requires complex and bulky systems that are not easily transportable and compatible with harsh combustion or field environments.
A viable alternative is performing DCS with electro-optically (EO) generated combs, which use ruggedized integrated optical devices designed for long-term operation in fiber optic communication systems.
While EO combs have a narrower spectral extension, reducing the number of detectable chemicals at once, their lower number of comb modes allows for much higher acquisition speeds, which is advantageous for studying transient phenomena.
This thesis builds on recent advancements in electro-optic technology to develop a robust and compact DCS platform for ultrafast, chemically-resolved analysis of several molecular species relevant to combustion studies. It introduces the novel combination of a Single-Sideband Modulator (SSM) and an Arbitrary Waveform Generator (AWG) to synthesize a dual comb in a single-path, fully-fibered configuration extending over 25 GHz for high-speed absorption measurements.
During this research, substantial effort was dedicated to several critical aspects aimed at advancing the development of a robust dual-comb spectrometer for ultrafast chemical

analysis. First of all the focus was on the identification of the optimal methods for generating electro-optic (EO) with high throughput and spectral flatness.
By understanding the intricate properties of SSMs, it was possibile to pinpoint the conditions under which these modulators perform best, ensuring that the EO comb generation is efficient and maintain a consistent spectral uniformity.

The second phase of this work involved synthesizing and characterizing the electric signal necessary for an Arbitrary Waveform Generator (AWG) to produce these EO combs. This step was crucial because the quality and precision of the electric signal directly impact the performance of the dual-comb spectrometer.
By meticulously creating and analyzing the required waveforms, the AWG was able to generate EO combs with the desired characteristics. This process included fine-tuning the parameters to achieve the best possible results, thus laying a solid foundation for the spectrometer's functionality.

Finally, an electronic board was designed to provide the correct voltage bias for an OEM SSM modulator and assembled on a prototypical breadboard. This component was essential for integrating the various elements of the setup and ensuring their seamless operation. The different parts of the system were completely tested to verify their performance and compatibility. This included validating the electronic board's ability to deliver stable and accurate voltage biases, which is vital for the consistent operation of the SSM modulator. Through these comprehensive tests, the setup could reliably generate EO combs and operate under the desired conditions.

These combined efforts culminated in a well-engineered system that integrates cutting-edge electro-optic technology with precise electronic control.
The results of this work have significantly advanced the potential for using dual-comb spectroscopy in various applications, particularly in fields requiring rapid and accurate chemical analysis.
Thanks to the developments at both the simulation and hardware levels during this thesis, a dual-comb EO spectrometer is nearly ready for operation and testing at telecom wavelengths. Compared to traditional spectrometers based on tunable continuous-wave lasers, this setup is expected to offer a significantly increased acquisition rate and a higher signal-to-noise ratio per spectral point and per unit of measurement time.
In the future, using nonlinear optics process the dual-comb source could be a shifted to the mid-IR region, the so called fingerprint region, where the fundamental molecular transition lies.
This adaptation would enhance sensitivity thanks to stronger fundamental rovibrational lines, which are important for medical, atmospheric, and combustion process analysis.

1 | Principles of Molecular Spectroscopy

This section deals with the interaction between an electromagnetic field of a light source and an ensemble of particles (atoms or molecules) through the semi-classical theory, with the purpose of obtaining an expression of the absorption coefficient of a given medium as a function of frequency. The following discussion regards an electric dipole interaction, but the general formalism can be applied also to other kinds of transitions.

1.1. Light Matter Interaction

A light beam is a traveling electromagnetic wave with an electric component represented by the expression:

$$E(z,t) = E_0 \cos(\omega t - kz) \tag{1.1}$$

where ω is the frequency of the oscillation and

$$k = |\vec{k}| = \frac{\omega n}{c}|\vec{u_z}| \tag{1.2}$$

is the propagation wave-vector. The mean intensity is:

$$I = \frac{1}{2} c n \varepsilon_0 E_0^2 \tag{1.3}$$

When laser radiation interacts with a mixture of atoms or molecules in a gas phase, the intensity decreases according to the Lambert-Beer law [1, 2]:

$$I(z) = I_0 e^{-\alpha z} \tag{1.4}$$

where I_0 is the input intensity in $\mathrm{W/m^2}$ and α is the absorption coefficient in $\mathrm{cm^{-1}}$.

The absorption is a frequency-dependent quantity that turns out to be proportional to the particle concentration n (cm^{-3}) and to an effective absorption area σ (cm^2) called cross-section:

$$\alpha(\omega) = n\sigma(\omega) \tag{1.5}$$

The rigorous approach for determining the absorption properties of an ensemble of particles involves the quantization of both the medium and the electromagnetic field. But a good model can also be obtained by the so-called semi-classical approach, which treats the particles from a quantum-mechanical point of view whereas the electromagnetic field of the light source is described by photons, that behave both as waves and particles, without specifying their quantum nature [3]. The formalism considers that the electrons of atoms or molecules can perform transitions to other energy levels in the presence of absorption or stimulated emission of a photon. Spontaneous emission and non-radiative processes are neglected and have to be added a posteriori. Thanks to the semi-classical approach, it is possible to retrieve the transition probabilities and the population density changes induced by the interaction between the electrons in the medium and the field.

The starting point is the perturbation theory, where the effects of the interacting field are considered as perturbation terms to be added to the unperturbed condition since they are much smaller than the Coulomb interactions of the nuclei. The electron distributions in the medium are treated with their perturbed wave-functions. They can be written in Dirac's notation as linear combinations of the wave-functions of the eigen-states in the unperturbed condition, $|\psi_n\rangle$, with time-dependent weighting factors $C_n(t)$ due to the perturbation field:

$$|\Psi(t)\rangle = \sum_n C_n(t)|\psi_n\rangle \tag{1.6}$$

The interaction between the electrons of the medium and the electromagnetic field is considered as a perturbation term $\hat{H}'$ of the unperturbed Hamiltonian $\hat{H}_0$:

$$\hat{H} = \hat{H}_0 + \hat{H}' \tag{1.7}$$

The unperturbed Hamiltonian provides the eigenstate wave-functions $|\psi_n\rangle$ by the Schrödinger equation:

$$\hat{H}_0|\psi_n\rangle = i\hbar\frac{\partial|\psi_n\rangle}{\partial t} \tag{1.8}$$

whereas the perturbation, in the weak-field approximation, can be calculated as the scalar product between the dipole moment of the medium and the electric field:

$$\hat{H}' = -\vec{\mu}\cdot\vec{E} \tag{1.9}$$

The total interaction Hamiltonian is a Hermitian operator, which means that it is equal to its eigen-operator $H^\dagger$ defined as

$$\langle\psi|\hat{H}|\phi\rangle = \langle\phi|\hat{H}^\dagger|\psi\rangle^* \tag{1.10}$$

For this kind of operators, the diagonal matrix elements are real numbers $H_{ii}^\dagger = H_{ii}^* = H_{ii}$ (related to physical observables) and the off-diagonal elements are complex conjugates $H_{ij}^\dagger = H_{ji}^* = H_{ij}$. Usually, the description begins with the case of two-level systems, where the electrons of the medium perform transitions from the ground to the excited state level. In general, two different approaches can be followed: the first is to write the rate equations of the population densities of the two levels and solve them to obtain the joint density of states in the presence of emission and absorption processes. The second is to exploit the properties of a quantum mechanical operator, the density matrix, applied to the interaction Hamiltonian. The last formalism is considered more versatile and is explained in the following subsection.

1.1.1. Density Matrix Approach for a Two-Level System

The density matrix provides an alternative to the wave-function for describing the state of a quantum mechanical system, with practical benefits for handling time evolution. It is defined as:

$$\hat{\rho} \equiv |\Psi(t)\rangle\langle\Psi(t)| \tag{1.11}$$

This operator is hermitian, and its trace, when applied to a physical quantity A, gives the expectation value of that quantity:

$$\langle A\rangle = \mathrm{Tr}(\hat{\rho}A) \tag{1.12}$$

Equation (1.12) serves as a "bridge" between the classical observable $\langle A\rangle$ and quantum mechanics (where ρ is a quantum mechanical operator). For a system in a pure state characterized by a single wave-function, $\langle\psi_n|\hat{\rho}|\psi_n\rangle$ represents the probability of finding the system in that particular $|\psi_n\rangle$ state. In a perturbed system described by the wave-functions $|\Psi(t)\rangle = \sum_n C_n(t)|\psi_n\rangle$, the density matrix elements are:

$$\rho_{nm} = \langle\psi_n|\hat{\rho}|\psi_m\rangle = \sum\langle\psi_n|\Psi(t)\rangle\langle\Psi(t)|\psi_m\rangle = C_n(t)C_m^*(t) \tag{1.13}$$

Here, the diagonal elements $\rho_{nn} = C_n C_n^* = p_n$ represent the probability of the system being in state $|\psi_n\rangle$, while the off-diagonal elements $\rho_{nm} = C_n(t)C_m^*(t) = C_n C_m^* e^{-i\omega_{nm}t}$ describe the coherent superposition between states $|\psi_n\rangle$ and $|\psi_m\rangle$.

A key property of the density matrix is its partial time derivative $\frac{\partial\hat{\rho}}{\partial t}$, which is directly proportional to the commutator of the density matrix and another operator, the interaction Hamiltonian:

$$\frac{\partial\hat{\rho}}{\partial t} = -\frac{i}{\hbar}[\hat{H}, \hat{\rho}] = \frac{i}{\hbar}(\hat{H}\hat{\rho} - \hat{\rho}\hat{H}) \tag{1.14}$$

Consider a two-level system with energies ϵ_1 and ϵ_2 and total electron population density N. An electron transition occurs if the incoming photon frequency is close to the resonance condition $\omega \approx \omega_0$ where $\omega_0 = (\epsilon_2 - \epsilon_1)/\hbar$. The system, assumed to be in quasi-equilibrium with both ground and excited states populated, can be pumped by electrical or optical methods. The density matrix for this two-level system is:

$$\hat{\rho} = \begin{pmatrix} \rho_{11} & \rho_{12} \\ \rho_{21} & \rho_{22} \end{pmatrix} \tag{1.15}$$

with $\rho_{12} = \rho_{21}^*$. The population of the ground state level is $N_1 = N\rho_{11}$ and of the excited state $N_2 = N\rho_{22}$. The population density difference is $\Delta N = N(\rho_{22} - \rho_{11})$.

The interaction Hamiltonian is the sum of the unperturbed Hamiltonian:

$$\hat{H}_0 = \begin{pmatrix} \epsilon_1 & 0 \\ 0 & \epsilon_2 \end{pmatrix} \tag{1.16}$$

and the perturbation Hamiltonian:

$$\hat{H}' = -\vec{\mu} \cdot \vec{E} = -\mu E = \begin{pmatrix} 0 & -\mu_{12}E \\ -\mu_{21}E & 0 \end{pmatrix} \tag{1.17}$$

Since the dipole moment is an even operator, the perturbation Hamiltonian contains only off-diagonal elements $\mu_{12}E = \mu_{21}^* E = \mu E$. Using Eq.(1.11), the expectation value of the dipole moment $\langle\hat{\mu}\rangle$ is:

$$\langle\hat{\mu}\rangle = \mathrm{Tr}(r\hat{h}o\hat{\mu}) = \mu(\rho_{12} + \rho_{21}) = \mu(\rho_{21}^* + \rho_{21}) = 2\mu\mathrm{Re}(\rho_{21}) \tag{1.18}$$

The term ρ_{21} relates to the coherence of the dipole moment oscillation, translating macroscopically into polarization $P = N\langle\hat{\mu}\rangle = 2N\mu\mathrm{Re}(\rho_{21})$.

The density matrix formalism uses Eq. (1.14) to derive the evolution of the matrix elements, representing the population densities of the two levels and the coherence of the dipole moment oscillation. The commutator between the density matrix and the Hamiltonian is:

$$[\hat{\rho}, \hat{H}] = \begin{pmatrix} \rho_{11} & \rho_{21}^* \\ \rho_{21} & \rho_{22} \end{pmatrix} \begin{pmatrix} \epsilon_1 & -\mu_{21}^* E \\ -\mu_{21} E & \epsilon_2 \end{pmatrix} - \begin{pmatrix} \epsilon_1 & -\mu_{21}^* E \\ -\mu_{21} E & \epsilon_2 \end{pmatrix} \begin{pmatrix} \rho_{11} & \rho_{21}^* \\ \rho_{21} & \rho_{22} \end{pmatrix} \tag{1.19}$$

which simplifies to:

$$\begin{pmatrix} (\rho_{21} - \rho_{21}^*)\mu E & -\rho_{21}^*(\epsilon_1 - \epsilon_2) - \mu E(\rho_{11} - \rho_{22}) \\ \rho_{21}^*(\epsilon_1 - \epsilon_2) + \mu E(\rho_{11} - \rho_{22}) & (\rho_{21}^* - \rho_{21})\mu E \end{pmatrix} \tag{1.20}$$

Using Eq. (1.14), we get:

$$\frac{\partial \rho_{21}}{\partial t} = \frac{i}{\hbar}[\rho_{21}(\epsilon_1 - \epsilon_2) + \mu E(\rho_{11} - \rho_{22})] \tag{1.21}$$

$$\frac{\partial \rho_{11}}{\partial t} = \frac{i}{\hbar}\mu E(\rho_{21} - \rho_{21}^*) \tag{1.22}$$

$$\frac{\partial \rho_{22}}{\partial t} = -\frac{i}{\hbar}\mu E(\rho_{21} - \rho_{21}^*) \tag{1.23}$$

These can be grouped and simplified by introducing $\epsilon_1 - \epsilon_2 = -\hbar\omega_0$:

$$\frac{\partial \rho_{21}}{\partial t} = -i\omega_0\rho_{21} + \frac{i\mu E}{\hbar}(\rho_{11} - \rho_{22}) \tag{1.24}$$

$$\frac{\partial(\rho_{11} - \rho_{22})}{\partial t} = \frac{2i\mu E}{\hbar}(\rho_{21} - \rho_{21}^*) \tag{1.25}$$

The first equation, without perturbation (i.e., $E = 0$), has the solution $\rho_{21}(t) = \rho_{21}(0)e^{-i\omega_0 t}$, indicating indefinite coherent oscillation. This unrealistic result requires a decay term $-\rho_{21}/T$, where T is the time constant related to spontaneous emission, to be added.

The second equation requires a decay term $-[(\rho_{11}-\rho_{22})-(\rho_{11}-\rho_{22})_{eq}]/\tau$ to return to equilibrium, where τ is typically shorter than T.

Rewriting ρ_{21} as $\rho_{21}=\sigma_{21}e^{-i\omega t}$, with σ_{21} varying slowly with time and $e^{-i\omega t}$ representing the dipole moment oscillation, and introducing decay terms, Eq.(1.23) and Eq.(1.24) become:

$$\frac{\partial\sigma_{21}}{\partial t}=i(\omega-\omega_0)\sigma_{21}+\frac{i\mu E_0}{2\hbar}-\frac{\sigma_{21}}{T} \tag{1.26}$$

$$\frac{\partial(\rho_{11}-\rho_{22})}{\partial t}=\frac{i\mu E_0}{\hbar}(\sigma_{21}-\sigma_{21}^*)-\frac{(\rho_{11}-\rho_{22})-(\rho_{11}-\rho_{22})_{eq}}{\tau} \tag{1.27}$$

In the stationary condition that we are interested in, one can set $\frac{\partial(\rho_{11}-\rho_{22})}{\partial t}=0$ and obtain the following system:

$$i(\omega-\omega_0)\sigma_{21}+i\frac{\mu E_0}{2\hbar}-\frac{\sigma_{21}}{T}=0 \tag{1.28}$$

$$i\frac{\mu E_0}{\hbar}(\sigma_{21}-\sigma_{21}^*)-\frac{(\rho_{11}-\rho_{22})-(\rho_{11}-\rho_{22})_{eq}}{\tau}=0 \tag{1.29}$$

with solutions:

$$\mathrm{Re}(\sigma_{21})=\frac{\Omega T}{2}\frac{(\omega_0-\omega)(\rho_{11}-\rho_{22})_{eq}}{1+(\omega-\omega_0)^2T^2+\Omega^2T\tau} \tag{1.30}$$

$$\mathrm{Im}(\sigma_{21})=\frac{\Omega T(\rho_{11}-\rho_{22})_{eq}}{1+(\omega-\omega_0)^2T^2+4\Omega^2T\tau} \tag{1.31}$$

$$(\rho_{11}-\rho_{22})=\frac{(\rho_{11}-\rho_{22})_{eq}}{1+(\omega-\omega_0)^2T^2+\Omega^2T\tau} \tag{1.32}$$

where the quantity Ω is defined as $\frac{\mu E_0}{\hbar}$ and is called Rabi frequency. The population difference ΔN may be then deduced as:

$$\Delta N=N(\rho_{11}-\rho_{22})=\frac{\Delta N_{eq}}{1+(\omega-\omega_0)^2T^2+\Omega^2T\tau} \tag{1.33}$$

According to Eq.(1.17), the electric dipole moment takes the form:

$$\langle\mu\rangle=2\mu\mathrm{Re}(\rho_{21})=2\mu(\mathrm{Re}(\sigma_{21})\cos(\omega t)+\mathrm{Im}(\sigma_{21})\sin(\omega t)) \tag{1.34}$$

and this results in a polarization:

$$P = N\langle\hat{\mu}\rangle = \frac{\mu^2 \Delta N_{eq} T}{3\hbar} E_0 \frac{\sin(\omega t) + (\omega_0 - \omega)T\cos(\omega t)}{1 + (\omega - \omega_0)^2 T^2 + 4\Omega^2 T\tau} \tag{1.35}$$

where for generality μ and E are no more considered parallel and the factor $\frac{1}{3}$ comes from the average over all orientations. P contains all the information of the interaction between the medium and the field and is also a classical physical observable. In the approximation of weak field the term $4\Omega^2 T\tau \ll 1$ and it can be considered negligible.

Comparing Eq.(1.34) with the macroscopic definition of polarization as a function of the linear susceptibility χ:

$$P = \mathrm{Re}(\varepsilon_0 \chi E_0 e^{i\omega t}) = \mathrm{Re}[\varepsilon_0(\chi' - i\chi'')E_0(\cos(\omega t) + i\sin(\omega t))] \tag{1.36}$$

it is possible to determine the real χ' and imaginary part χ'', in particular the first is related to dispersion effects and the second to absorption effects:

$$\chi'(\omega - \omega_0) = -\frac{\mu^2 \pi}{\varepsilon_0 \hbar} T \Delta N_{eq}(\omega - \omega_0) \left[\frac{T}{\pi[1 + (\omega - \omega_0)^2 T^2]}\right] \tag{1.37}$$

$$\chi''(\omega - \omega_0) = \frac{\mu^2 \pi}{\varepsilon_0 \hbar} \Delta N_{eq} \left[\frac{T}{\pi[1 + (\omega - \omega_0)^2 T^2]}\right] \tag{1.38}$$

The Lorentzian function in parenthesis can be indicated as $g(\omega - \omega_0)$ and is characterized by a normalized area $\left(\int_{-\infty}^{+\infty} g(\omega - \omega_0) d\omega = 1\right)$. Notice that $g(\omega - \omega_0)$ acts as a source of broadening of the transition, as this can be driven also when $\omega \neq \omega_0$.

To retrieve the absorption coefficient of the medium, let us recur to the definition of the relative dielectric constant of the medium, related both to the resonant $\chi(\omega)$ and non-resonant χ_{nr} susceptibility by:

$$\varepsilon_r = 1 + \chi_{nr} + \chi(\omega - \omega_0) = n^2 + \chi(\omega - \omega_0) = n^2 \left(1 + \frac{\chi(\omega - \omega_0)}{n^2}\right) = n_T^2 \tag{1.39}$$

with n being the refractive index and n_T the total refractive index. Under the assumption $\frac{\chi(\omega - \omega_0)}{n^2} \ll 1$ the total refractive index may be approximated by $n_T = n\left[1 + \frac{\chi(\omega)}{2n^2}\right]$ and the total wave-vector, since $\omega - \omega_0 \ll \omega_0$ even considering all the de-phasing sources, is

expressed as:

$$k_T \approx \frac{\omega_0 n_T}{c} = \frac{\omega_0 n}{c}\left(1 + \frac{\chi(\omega-\omega_0)}{2n^2}\right) = \frac{\omega n}{c}\left(1 + \frac{\chi'}{2n^2} - i\frac{\chi''}{2n^2}\right) = k' + k'' \tag{1.40}$$

From Eq. 1.39, the electromagnetic field inside the medium after a propagation distance z may be written as:

$$E = E_0 e^{i(\omega t - k_T z)} = E_0 e^{i(\omega t - k' z)} e^{-k'' z} \tag{1.41}$$

where the term $e^{-k''z}$ accounts for an exponential decay of the field amplitude with a decay rate $\alpha = -2k''$ given by

$$\alpha(\omega-\omega_0) = k\frac{\chi''(\omega)}{n^2} = k\frac{\mu^2\pi}{\varepsilon_0\hbar}\Delta N_{eq} g(\omega-\omega_0) = \frac{\omega_0}{c}\frac{\mu^2\pi}{\varepsilon_0\hbar}\Delta N_{eq} g(\omega-\omega_0) \tag{1.42}$$

which depends on the square of the transition dipole moment μ^2 and the total population difference $\Delta N = \Delta N_{eq} g(\omega-\omega_0)$.

The absorption coefficient $\alpha(\omega-\omega_0)$ is usually expressed in a more concise form:

$$\alpha(\omega-\omega_0) = \sigma(\omega-\omega_0)\Delta N_{eq} \tag{1.43}$$

where $\sigma(\omega-\omega_0)$ is called absorption cross-section, taking the role of the effective absorption area used in the phenomenological description. By doing the modulus square of $E = E_0 e^{i(\omega t - k' z)} e^{-\alpha z/2}$ to obtain the intensity during propagation through the medium, the Lambert-Beer law is retrieved. $g(\omega-\omega_0)$ is an intrinsic broadening of the transition line, representing the loss of coherence between the oscillation of the dipole moment and the electromagnetic field due to spontaneous emission, called natural broadening. When other mechanisms are present, $g(\omega-\omega_0)$ comprises them resulting in a broader profile, as shown in the next subsection.

1.1.2. Spectral Line Intensity of Molecules

Let's consider a transition between two levels of a molecular gas sample. Starting from Eq. 1.43, the absorption coefficient $\alpha(\omega-\omega_0)$ can be expressed as

$$\alpha(\omega-\omega_0) = nSg(\omega-\omega_0) \tag{1.44}$$

where n is molecular density expressed in molecules/cm^3, S represents the line intensity

in $\mathrm{cm}^{-1}/\mathrm{molecule}\cdot\mathrm{cm}^{-2}$, and $g(\omega-\omega_0)$ is the normalized line shape function expressed in cm: The difference in the electron population density ΔN is proportional to the molecular density n. As will be shown below, the line strength S represents the intensity of the spectrum, including all the parameters of the transition, while the normalized line shape profile $g(\omega-\omega_0)$ accounts for all broadening mechanisms.

At equilibrium the electron population density of i-th energy level is expressed through the Boltzmann distribution:

$$N_i = p_i(T) n e^{-\frac{\epsilon_i}{k_B T}} \tag{1.45}$$

where T is the gas temperature and $p_i(T)$ is a statistical weight of the partition function at temperature T [4, 5]. From Eq. 1.45, the difference in population densities of a two-level system can be calculated as:

$$\Delta N = n\left[p_1(T)e^{-\frac{\epsilon_1}{k_B T}} - p_2(T)e^{-\frac{\epsilon_2}{k_B T}}\right] = nf(T) \tag{1.46}$$

The line intensity S is a fundamental parameter of the transition. It depends on temperature, and includes all the information about the transition (required photon energy, whether it is an electric dipole or quadrupole transition, etc.). Without describing the complete analytical procedure, provided elsewhere [6], a full expression for the line strength is derived from the rate equations of population densities introducing the Einstein coefficient A_{21}:

$$S = \frac{A_{21}\pi p_2(T)}{2c\omega_0^2} e^{\frac{hc\epsilon_1}{k_B T}} \left(1 - e^{-\frac{hc\omega_0}{k_B T}}\right) \tag{1.47}$$

If Einstein coefficient is used to express line intensity, this becames independent of the type of transition, whether it is electric dipole, magnetic dipole, or electric quadrupole. Specifically, since the spectroscopic investigations presented in this thesis involve electric dipole transitions, it is useful to write the explicit dependence of μ_{21} as a function of the Einstein coefficient:

$$mu_{21} = \sqrt{\frac{A_{21} 3\epsilon_0 hc^3}{2\omega_0^3}} \tag{1.48}$$

In the HITRAN database, line intensity coefficients are tabulated for various molecules and isotopes at $T = 296$ K. Starting from this coefficient is possible to retrieve line

intensities values at a different T. The integral of the absorption coefficient to obtain the integrated absorption area (defined as the area under the absorption curve) divided by the molecular density allows to retrieve e the line intensity parameter from experimental measurements:

$$S = \frac{\int_{-\infty}^{+\infty} \alpha(\omega - \omega_0) d\omega}{n} = \frac{Area}{n} \tag{1.49}$$

1.2. Line Broadening Mechanisms

As already mentioned earlier, the last term of Eq. 1.44 is the function $g(\omega - \omega_0)$ which accounts for all broadening mechanisms causing a deviation from the delta function shape of the line. Such a broadening mechanisms can be divided into two classes: homogeneous mechanisms, which increase the width of the line-shape of every atom or molecule in the ensemble in the same way and are characterized by a Lorentzian line-shape, and inhomogeneous mechanisms, which distribute the effective resonance frequencies of the ensemble around a central value ω_0 represented by Gaussian functions.

1.2.1. Homogeneous Broadening Mechanisms

Eqs. 1.42 and 1.44 address the natural broadening of the absorption spectrum caused by spontaneous decays of an excited state. These events lead to a loss of coherence between the oscillations of the dipole moments and the interacting external field. Natural broadening can be understood using the model of a damped oscillator, represented by the equation:

$$\frac{d^2x}{dt^2} + \frac{1}{T}\frac{dx}{dt} + \omega_0^2 x = 0 \tag{1.50}$$

where T is the decay time constant, also known as the natural lifetime. The solution to this equation is:

$$x(t) = x_0 \cos(\omega_0 t + \phi_0) e^{-t/T} \tag{1.51}$$

where x_0 and ϕ_0 are the initial position and phase, respectvely. The Fourier transform of this solution is a broadened Lorentzian profile centered at ω_0:

$$g(\omega - \omega_0) = \frac{T}{\pi[1 + (\omega - \omega_0)^2 T^2]} \tag{1.52}$$

where $\Delta\omega_{FWHM} = \frac{2}{T}$ corresponent to $\Delta\nu_{FWHM} = \frac{2}{2\pi T}$: the meaning od pedices FWHM refers to the fact that the linewidth is evaluated at Full Width at Half Maximum. Natural

broadening affects each atom or molecule in the ensemble in the same way , setting a fundamental lower limit to the spectral linewidth.

A second homogeneous broadening mechanism arises from elastic collisions between atoms or molecules, known as collisional or pressure broadening. The pressure of a moecolar gas samples is directly proportional to the particle density and then to the probability of collision. The analytical treatment of collisional broadening assumes collisions occurring at times $t_1, t_2, t_3, \ldots$ spaced by intervals τ. This last one is a random variable with an expected value τ_c and probability distribution given by [7]:

$$\frac{1}{\tau_c} \exp\left(-\frac{\tau}{\tau_c}\right) \tag{1.53}$$

Collisions are assumed to be elastic, and then each collision causes random phase jumps in the transition probability. Under these assumptions, the interaction between the electric field and the colliding molecules can be treated as the interaction with a monochromatic field experiencing random phase jumps, with no collisions in the ensemble. The electric field has a phase that varies randomly every τ seconds:

$$E(t) = E_0 \cos(\omega_0 t + \phi(t)) = \frac{E_0}{2}\left(e^{i\omega_0 t + \phi(t)} + e^{-i\omega_0 t - \phi(t)}\right) \tag{1.54}$$

Here, $\phi(t)$ is constant within the intervals between collisions. The mean time between collisions τ_c can be derived from the kinetic theory of gases, where atoms and molecules are modeled as rigid spheres with mass m and radius a. For a given temperature T and pressure p, τ_c is:

$$\tau_c = \frac{\sqrt{m k_B T}}{16\sqrt{\pi} a^2 p} \tag{1.55}$$

Collisions also cause a shift $\delta\omega$ in the absorption distribution's central value ω_0, due to inter-particle interactions altering energy levels based on molecular distance. [8]

The broadening function $g(\omega - \omega_0)$, derived using the density matrix formalism, is the convolution of two Lorentzian profiles: $\gamma_{n_{FWHM}} = 1/T$ from the natural lifetime and $\gamma_{c_{FWHM}} = 2/\tau_c$ from collisions. Consequently, the spectral profile considering both natural and collisional broadening is:

$$g(\omega - \omega_0) = \frac{\left(\frac{\gamma_n}{2} + \frac{\gamma_c}{2}\right)^2}{\pi\left[\left(\frac{\gamma_n}{2} + \frac{\gamma_c}{2}\right)^2 + (\omega - \omega_0 + \delta\omega)^2\right]} \tag{1.56}$$

It is important to point out that γ_c is directly proportional to the gas pressure by means

of a constant, called C_p [9], and for every molecular sample it can be written as $\gamma_c = C_p p$. A reduction of the self-induced collisional broadening thus can be controllable regulating the sample pressure p. Collisional broadening usually dominates the natural broadening and then this last contribution that can be neglected.

A third homogeneous broadening is caused by particle collisions with the wall of the containing cell, called wall-collision broadening. This broadening is analysed with the kinetic theory of gases and the Maxwell-Boltzmann distribution of the molecular speed. It can be demonstrated that the FWHM of the function $g(\omega - \omega_0)$ increases by the factor:

$$\gamma_w = \frac{\bar{v}}{2\pi D} \tag{1.57}$$

where $\bar{v} = \sqrt{\frac{8k_B T}{\pi m}}$ is the averaged speed and D is the cell diameter. This broadening can be controlled easily since it is inversely proportional to the diameter D.

The last broadening mechanism usually included in the homogeneous class is due to the finite interaction time of molecules and the laser probe. Every beam is characterized by a finite diameter and moving molecules than interacts with the laser beam only during the crossing time of the beam. The consequent broadening is then related with the non infinite interaction time between light and sample and for this reason is named transit-time broadening. If the spontaneous lifetime T of a transition is longer than $\tau_t = \frac{a}{\bar{v}}$ (a being the beam diameter), which is the time of the interaction between moving molecules and the light beam, the transition linewidth is increased because of the uncertainty between a function and its Fourier transform. The transit time effect can be treated as an electric field oscillation that suddenly stops when interacting with the molecular sample with a resulting contribution of:

$$\gamma_t = \frac{\bar{v}}{2\pi a} \tag{1.58}$$

It has to be noticed that the transit-time broadening is a homogeneous broadening mechanism with a Lorentzian shape only at a first order approximation, i.e., when the velocity distribution may be assumed peaked around the mean value and the interacting beam is simplified with a planar wave front. When the curvature of the phase front of the light beam and the Maxwell-Boltzmann velocity distribution are taken into account, the transit-time broadening is inhomogeneous and characterised by an asymmetric and distorted Lorentzian shape. Indeed molecules have different interaction times with the beam depending on their velocity distribution, in particular with its absolute value and direction.

1.2.2. Inhomogeneous Broadening Mechanisms

The primary broadening mechanism that limits the resolution of spectroscopic measurements in the IR for gas samples at low pressures and room temperature is caused by the thermal motions of particles, known as Doppler broadening. Doppler broadening is an inhomogeneous broadening mechanism that varies from molecule to molecule and depends on the temperature T. While other inhomogeneous mechanisms can exist, they are generally negligible in the gas phase, making Doppler broadening the dominant process. This effect occurs due to the kinetic energy of molecules interacting with the electric field.

Consider an electric field propagating in the z-direction of a three-dimensional space with an angular frequency ω. If a molecule moves in the same direction as the field, it experiences a different angular frequency ω' given by:

$$\omega' = \omega \left(1 - \frac{v_z}{c}\right) \tag{1.59}$$

where c is the speed of light and the molecular velocity $v_z \ll c$. For a two-level system, absorption occurs when $\omega' = \omega_0$, leading to an effective transition angular frequency ω_0':

$$\omega_0' = \omega_0 \left(1 - \frac{v_z}{c}\right) \approx \omega_0 \left(1 + \frac{v_z}{c}\right) \tag{1.60}$$

This indicates that the resonance frequency of the molecule is no more $\omega_0 = (E_2 - E_1)/\hbar$ but is shifted by at a new ω_0' that results to be dependent of the speed of the interrogated molecule.

For all molecules in the ensemble, the probability distribution of the velocity component v_z for a gas at thermodynamic equilibrium is:

$$f(v_z) = \sqrt{\frac{m}{2\pi k_B T}} e^{-\frac{m v_z^2}{2 k_B T}} \tag{1.61}$$

It is possible to calculate the broadening $\Delta\omega$ of the absorption line integrating all the Doppler contribution of al the elementary classes of molecule speed. The density of particles with velocities between v_z and $v_z + dv_z$ is:

$$dN(v_z) = N f(v_z) dv_z \tag{1.62}$$

where N is the total molecular density. The resonance frequency of these particles is

within the interval $\omega_0', \omega_0' + d\omega_0'$ with $d\omega_0' = \frac{\omega_0}{c} dv_z$. Thus, $dN(v_z)$ can be expressed as:

$$dN(v_z) = Ng^*(\omega_0' - \omega_0)d\omega_0' \tag{1.63}$$

where $g^*(\omega_0' - \omega_0)$ is the Doppler broadening line-shape function:

$$g^*(\omega_0' - \omega_0) = \frac{dv_z}{d\omega_0'} f(v_z) = \frac{c}{\omega_0}\sqrt{\frac{m}{2\pi k_B T}} e^{-\frac{mc^2(\omega_0' - \omega_0)^2}{2k_B T \omega_0^2}} \tag{1.64}$$

where $v_z = \frac{c(\omega_0' - \omega_0)}{\omega_0}$.

In particular $g^*(\omega_0' - \omega_0)$ is a Gaussian function with FWHM:

$$\Delta\omega = 2\omega_0\sqrt{\frac{2k_B T \log(2)}{mc^2}} \Rightarrow \Delta\nu = 2\nu_0\sqrt{\frac{2k_B T \log(2)}{mc^2}} \tag{1.65}$$

This FWHM is the dominant factor when considering low-pressure gas samples. Eq. 1.65 is particularly significant because it links the optical absorption linewidth to the thermal energy $k_B T$, enabling the determination of the Boltzmann constant k_B by fixing the temperature or vice versa; this principle is at the basis of Doppler-Broadened Thermometry.

1.2.3. Voigt Profile

The Voigt profile serves as an effective model when multiple broadening mechanisms, including collisional effects, are present. In cases where Doppler broadening is the primary factor, it can be considered independent from collisional effects. The velocity distribution of molecules is still characterized by the Gaussian function, based on the Maxwell-Boltzmann distribution. This Gaussian component is then convolved with the Lorentzian contribution, resulting in a profile that is called Voigt profile:

$$g_{\text{tot}}(\omega - \omega_0) = g_L(\omega - \omega_0) \otimes g_G^*(\omega' - \omega_0) = \int_{-\infty}^{+\infty} g(\omega' - \omega_0) g^*(\omega - \omega') d\omega' \tag{1.66}$$

This profile accounts for both the Lorentzian g_L and Gaussian g_G broadening, as well as the pressure-induced shift of the central frequency.

Equation 1.66 assumes no correlation between collisional effects and the speed of the molecules. However, as pressure increases, the impact of collisions on velocity changes becomes significant and cannot be ignored. The Voigt profile in this case is no more sufficient to properly describe all the physical aspects that take place in the gaseous sample.

More refined profile have been then developed to take into account more subtle physical effects (e.g the speed dependent billiard ball profile the Hartmann-Tran profile,...), that impact on the absorption line shape but this is outside the scope of this thesis.

1.3. Molecular Energy Levels and Transitions in the IR Region

This subsection extends the previous treatment of transitions in two-level systems to the more complex case of molecular gas transitions. Here, the two energy levels involved in absorption are part of a structure comprising multiple energy levels, known as an energy band. This section focuses on the molecular energy level structure, particularly the IR-induced transitions studied in this thesis.

According to the quantum theory of molecules developed by Born and Oppenheimer [10], the Hamiltonian describing molecular motion is divided into four main terms:

$$\hat{H} = \hat{H}_{\text{electronic}} + \hat{H}_{\text{vibration}} + \hat{H}_{\text{rotation}} + \hat{H}_{\text{translation}} \tag{1.67}$$

These terms correspond to electronic, vibrational, rotational, and translational motions. The translational term is usually neglected as it does not interact with light beams. The dominant energy contribution comes from electronic motions, where transitions between electronic levels require photons with energies between 1 and 10 eV (visible and UV photons). Vibrational transitions involve photons with energies between 0.1 and 1 eV (near-IR and mid-IR photons). Rotational transitions need photons with energies between 0.0001 and 0.1 eV (microwave photons).

Following the Born-Oppenheimer approximation, during an energy level transition, atomic nuclei are considered stationary relative to the lighter electrons. Energy levels are calculated assuming fixed nuclear positions with potential energy depending on internuclear separation, typically represented by the Morse potential function.
In Figure 1.1 a graphical representation of the energy levels is provided.

1.3.1. Rotational Energy Levels

Molecules consist of atoms bound at stable distances, allowing the definition of the moment of inertia I:

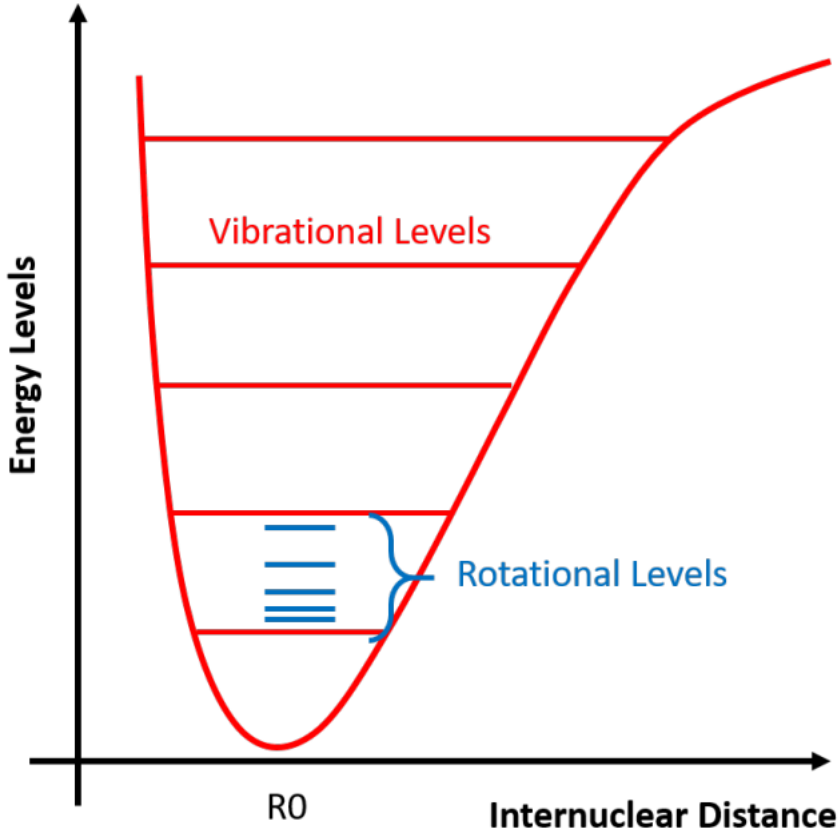

Figure 1.1: Rovibrational energy levels as a function of the internuclear distance. Rotational levels are coloured in blue, whereas vibrational are coloured in red.

$$I = \sum_{i=1}^{N} m_i r_i^2 \tag{1.68}$$

where m_i is the mass and r_i is the distance of the i-th atom from the rotational axis through the center of mass. The moment of inertia of electrons is negligible compared to that of the nuclei. For linear rotor molecules (e.g., diatomic or some polyatomic molecules like HCl, CO, CO_2), the reduced mass μ is:

$$\frac{1}{\mu} = \sum_{i=1}^{N} \frac{1}{m_i} \tag{1.69}$$

and the system can be considered a single particle of mass μ rotating at distance r from the center of mass, with moment of inertia $I = \mu r^2$. The rotational energy can be calculated in a classical way as:

$$\epsilon_x = \frac{1}{2} I_x \omega_x^2 = \frac{L_x^2}{2I_x} \tag{1.70}$$

where $L = I\omega$ is the angular momentum. Quantum mechanically, the rotational Hamiltonian is:

$$H_x = \frac{L_b^2}{2I_x} \tag{1.71}$$

with the angular momentum operator taking quantized values based on the rotational quantum number $l = 0, 1, 2, \ldots$:

$$L_c^2 = \hbar^2 l(l+1) \tag{1.72}$$

yielding quantized energy levels:

$$\epsilon_{\text{rot}} = \frac{\hbar^2}{2I} l(l+1) \tag{1.73}$$

These levels are often $(2l+1)$-fold degenerate, the degeneracy can be lifted by applying a magnetic field, for instance, and the operator that lifts the degeneracy of energy levels is the projection of the angular moment to the vertical axis respect to the plane where the molecule lies, usually indicated with the letter z. L_{cz} can take only the following values:

$$L_{cz} = m\hbar \tag{1.74}$$

where m is a quantum number spacing from $\pm l$.

Within an electric dipole interaction, selection rules for Eqs 1.72,1.74 are obtained:

$$\Delta l = \pm 1; \Delta m = 0, \pm 1 \tag{1.75}$$

where the expression on the left side shows that transitions can happen only between adjacent levels with different l. The selection rule on the right side shows how other transitions are possible after lifting the $(2l+1)$-fold degeneracy.

The rigid rotor model is a simplification of a real molecule. More sophisticated models consider the atoms connected by elastic springs where distortions are included during the rotation of the system, in particular correction terms regarding the effect of centrifugal

forces. The rigorous treatment, reported for instance in [11], leads to a definition of the rotational energy levels as a series expansion of the term $l(l+1)$:

$$\epsilon_{rot} = hc\left[Bl(l+1) - Dl^2(l+1)^2 + Hl^3(l+1)^3 + Ll^4(l+1)^4\right] \tag{1.76}$$

where letters refer to specific spectroscopic constants: D takes into account bond distortions, H and L regard high-order corrections.

The previous quantum mechanical formalism can be applied to other systems with different geometries, for example for symmetric rotor molecules, spherical rotor molecules and so on.

1.3.2. Vibrational and Rovibrational Energy Levels

The potential function has a minimum at the equilibrium internuclear distance R_0. The Morse function approximates the real potential function near R_0, modeling the atomic bond as a spring. Solving the Schrödinger equation for a harmonic oscillator yields quantized vibrational energy levels:

$$\epsilon_{\text{vib}} = \left(v + \frac{1}{2}\right)\hbar\omega \tag{1.77}$$

with the zero-point energy for $v = 0$. The selection rule for vibrational transitions is $\Delta v = \pm 1$. The harmonic oscillator model is an approximation valid only for the first few levels; the Morse potential provides a more accurate description, allowing overtone transitions $\Delta v = \pm 2, \pm 3, \ldots$.

Rotational levels are included between vibrational levels, slightly altering molecular geometry. The combined rovibrational levels have energies:

$$\epsilon_{\text{rovib}} = hc\left(G_v + B_v l(l+1) - D_v l^2(l+1)^2 + H_v l^3(l+1)^3 + L_v l^4(l+1)^4\right) \tag{1.78}$$

Figure 1.2 illustrates three main branches of rovibrational transitions: P-branch ($\Delta l = -1$), R-branch ($\Delta l = +1$), and Q-branch ($\Delta l = 0$). These transitions are tabulated in the HITRAN database [9].

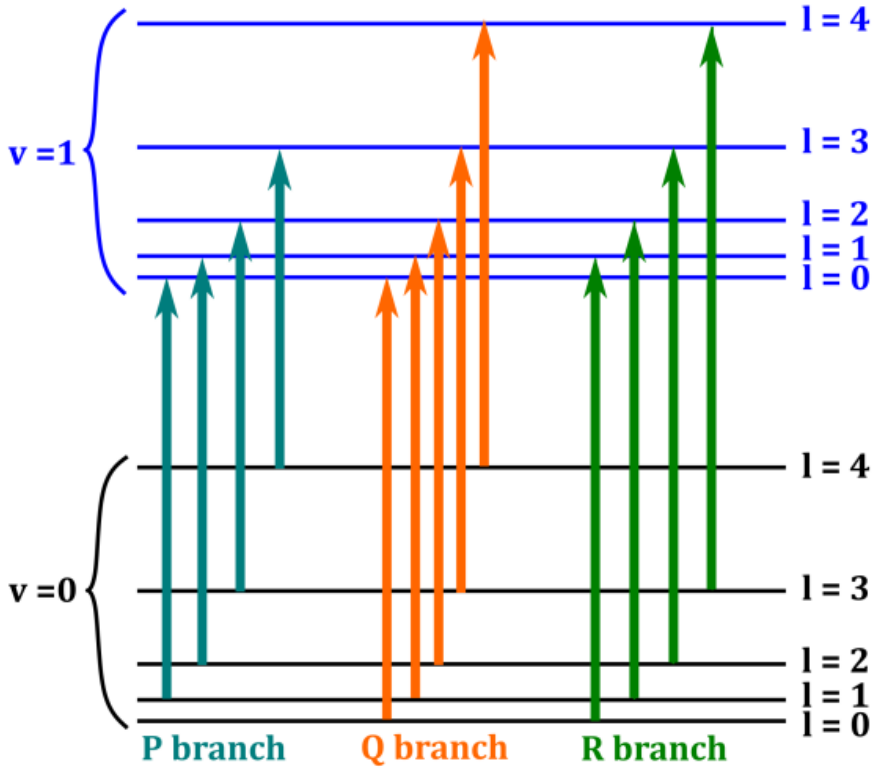

Figure 1.2: Rovibrational transitions between energy levels of a molecular system for the three branches P, Q and R.

2 | Electro Optic Dual Comb Spectroscopy

2.1. Optical Frequency Combs

Since the invention of mode-locked lasers in the early 1970s, their ability to produce optical pulses in the picosecond and femtosecond range has been utilized in time-resolved spectroscopy measurements.
It was only at the end of the 1990s that the first frequency comb was realized, a milestone that earned Theodor W. Hansch and John L. Hall the Nobel Prize in Physics in 2005. Since then, frequency combs have revolutionized many different field from optical clock to astrophysics, from medical diagnostics to molecular spectroscopy. In this last field, where the electro optical dual comb spectrometer subject of this thesis has the major impacts, frequency combs providing unprecedented precision and accuracy in detecting absorption lines.
Trace gas sensing has significantly improvements in sensitivity, broad spectral coverage, and high resolution when passive high-finesse optical cavities are combined with frequency combs used as probe or reference sources.

Frequency domain representation is useful to understand the spectral structure of frequency combs, crucial for the aforementioned advancements. In a mode-locked laser, an optical pulse train emerges when numerous longitudinal modes ν_n oscillate in phase due to a non-linear process, such as the non-linear optical Kerr effect. In the time domain, the coherent superposition of these modes produces a pulse circulating inside the optical cavity, partially transmitted each time it reaches the output mirror. This periodic transmission called pulse repetition rate, occurs every $T = \frac{2nL}{c}$ seconds, where L is the cavity length, n the refractive index, and c the speed of light.

The electric field $E(t)$ of a mode-locked laser can be mathematically expressed as a convolution of an envelope function $A_0(t)$, defining the individual pulse profile, with a series

of delta functions spaced by the period T:

$$E(t) = \left[A_0(t) * \sum_{m=-\infty}^{+\infty} \delta(t - mT) \right] e^{i2\pi\nu_0 t} \tag{2.1}$$

where the phase term $e^{i2\pi\nu_0 t}$ stems from the underlying carrier frequency ν_0.

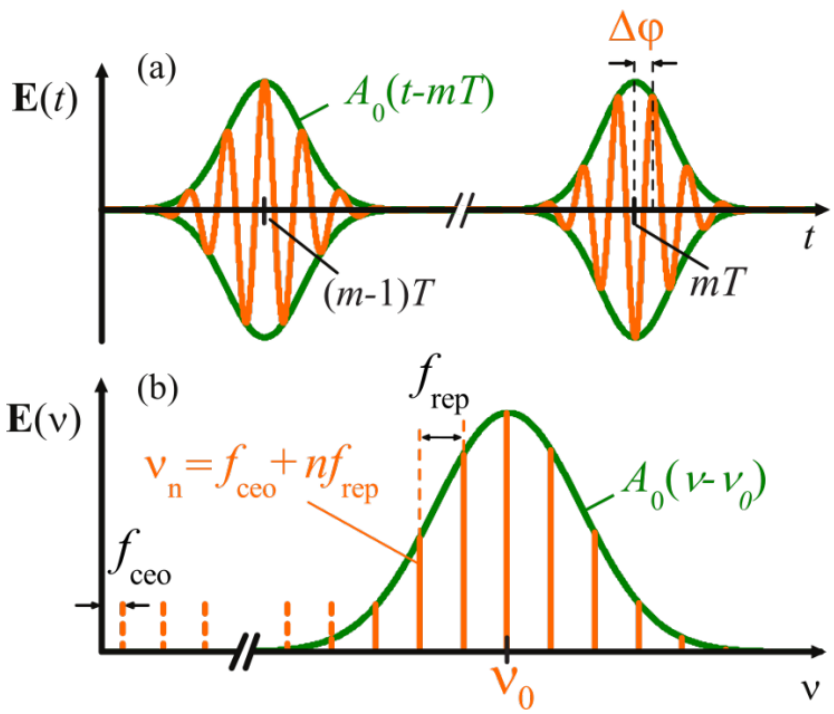

Figure 2.1: Time domain (a) and frequency domain (b) representation of the electrical field of a laser working in mode locking regime.

As shown in Figure 2.1(a), the carrier frequency typically undergoes phase slippage from pulse to pulse, disrupting the waveform's periodicity. This phase slippage $\Delta\varphi$ is mainly caused by the difference between phase and group velocity in the laser resonator due to dispersion.

A different perspective can be obtained if we look at the corresponding spectrum $E(\nu)$ that is calculated as the Fourier transform of Eq. 2.1:

$$E(v) = \mathcal{F}[E(t)] = \left[A_0(v) \sum_{k=-\infty}^{+\infty} \delta\left(v - \frac{k}{T}\right) \right] * \delta(v - v_0) \tag{2.2}$$

where $A_0(\nu)$ is the transform of $A_0(t)$. Introducing the laser repetition frequency $f_r = \frac{1}{T}$,

Eq.2.2 is rewritten as:

$$E(v) = A_0(\nu - \nu_0) f_r \sum_{k=-\infty}^{+\infty} \delta(\nu - \nu_0 - k f_r) \tag{2.3}$$

This spectrum, depicted in Figure 2.1(b), encomapsses different delta functions equally spaced by f_r, whose amplitudes are modulated by the spectral envelope $A_0(\nu - \nu_0)$. This delta functions are the modes of the lasers, also called comb teeth, that contemporary oscillates under the laser emission bandwidth. Defining an integer number n_0 and a radio-frequency (RF) f_{ceo} where the subscript means Carrier Envelop Offset (frequency), is possible to express every $\nu_0 = n_0 f_r + f_{ceo}$ with $0 < f_{ceo} < f_r$, and renumbering the summation in Eq.(2.3) with a new index $n = k + n_0$, a simple expression for the frequency domain spectrum is deduced:

$$E(v) = A_0(\nu - \nu_0) f_r \sum_{n=-\infty}^{+\infty} \delta(\nu - n f_r - f_{ceo}) = A_0(\nu_n - \nu_0) \tag{2.4}$$

where:

$$\nu_n = n f_r + f_{ceo} \tag{2.5}$$

Equation 2.5 shows that the comb is composed of different optical frequencies separated by f_r, which determines the mode spacing, while f_{ceo} represents the offset of the optical modes from the origin of the frequency axis, as sketched in Fig. 2.1(b). The number of oscillating optical frequencies can be roughly estimated by the ratio of the pulse optical bandwidth divided by f_r. Considering a mode-locked laser with a spectral bandwidth of 10 THz (pulses shorter than 100 fs) and f_r of 100 MHz, the number of optical modes is 10^6.

The physical origin of f_{ceo} arises from the aforementioned phase slippage $\Delta\varphi$ between the carrier frequency and the pulse envelope. To quantify $\Delta\varphi$ and relate it to f_{ceo} is possible to follow the approach reported in Ref. [12]. Let's consider two time instants separated by a pulse repetition period T, $t_m = mT$ and $t_{m-1} = (m-1)T$, corresponding to the adjacent envelope maxima in Figure 2.1(a). Let φ_m and φ_{m-1} be the respective values of the absolute phase of their electric fields. The phase slippage $\Delta\varphi$ is constant from pulse to pulse and is given by:

$$\Delta\varphi = \varphi_m - \varphi_{m-1} = 2\pi\nu_0 T = \frac{2\pi(n_0 f_r + f_{ceo})}{f_r} = \frac{2\pi f_{ceo}}{f_r} \tag{2.6}$$

showing that the time-domain phase shift from pulse to pulse between the carrier and the envelope corresponds in the frequency domain to a rigid offset by f_{ceo} of the whole comb spectrum.

One of the most important properties of a frequency comb, intrinsically implied in Eq. 2.5 is that both f_r and f_{ceo} in the second member belong the RF range and can be stabilized against a primary reference oscillator, such as a Cs clock. This way, the mode-locked laser becomes a frequency ruler called an Optical Frequency Comb (OFC), with thousands of optical modes ν_n whose absolute values are known to an accuracy corresponding to the error propagation of f_r and f_{ceo}. Therefore, a frequency comb is also depicted as the superposition of thousands of lasers emitting in phase at specific, determined frequencies.

Stabilizing f_r is relatively straightforward since the pulse repetition rate can be acquired by a fast photodetector and phase-locked to a primary reference by adjusting the cavity length of the oscillator, using a Piezo-Electric Transducer (PZT) mounted on one cavity mirror, or adjusting the phase by a fast intra-cavity Electro-Optic Modulator (EOM) [13]. However, detecting f_{ceo} remained the bottleneck for realizing a frequency comb synthesizer until the late 1990s. An experimental solution was found only in 1999, demonstrating that femtosecond pulses maintain their phase coherence when spectrally broadened in non-linear materials with strong third-order susceptibility $\chi^{(3)}$ [14]. The first direct optical-to-RF conversion was achieved using a complex scheme, involving a frequency divider imposing fixed ratios and the superposition of the 3.5^{th} and 4th harmonics of the mode-locked laser, as detailed in [15]. This task became significantly simpler with the advent of highly non-linear fibers, such as photonic crystal fibers, enabling the realization of an octave-spanning spectrum [16], i.e., a frequency spectrum where the higher frequencies are twice the lower ones. Such a spectrally broadened laser allows for direct measurement of f_{ceo} using the so called $f - 2f$ self-referencing scheme, where only the direct output of the laser is needed [17][18] without any frequency division. As shown in Fig. 2.2, the superposition of a frequency-doubled portion of the octave-spanning spectrum with the original spectrum on a photodetector generates a heterodyne beat-note signal between the $2\nu_n$ and the ν_m comb line, where $m = 2n$:

$$2\nu_n - \nu_m = 2(nf_r + f_{ceo}) - (2nf_r + f_{ceo}) = f_{ceo} \tag{2.7}$$

directly corresponding to the carrier-envelope offset frequency. f_{ceo} can then be phase-locked to a primary reference oscillator by adjusting the pump laser power [19] tilting the high reflector mirror in solid-state femtosecond oscillators [16] or driving an intracavity electro optic modulator, known methods for modifying intra-cavity dispersion and thus

the phase slippage.

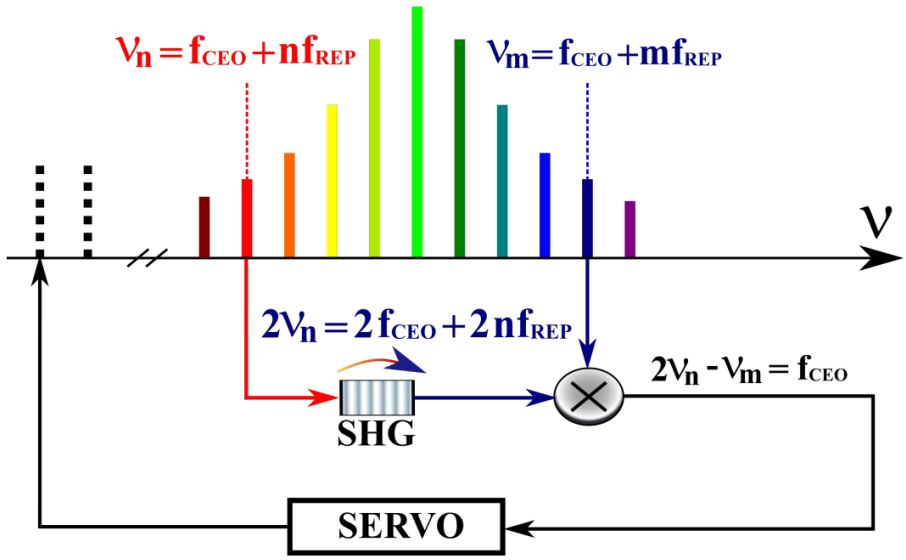

Figure 2.2: $f - 2f$ interferometer scheme. Heterodine beat note signal corresponding to f_{ceo} is obtained frequency doubling the red portion of an octave-spanning supercontinuum spectrum around ν_n and superimposing with the blue part ν_m. This signal is then compared with a reference radio-frequency signal and stabilized by a servo driving the laser pump power or an intracavity electro -optical modulator

2.2. Electro Optic Combs

To date, OFCs mainly consist of three types: MLLs, Kerr frequency combs (Kerr combs), and electro-optic frequency combs (E-O combs) [20]. Each type has distinct advantages and disadvantages, making them suitable for various applications.

MLLs are the oldest type of OFCs, forming the foundation of the fundamental principles of OFCs. MLLs can be divided into solid-state MLLs and fiber MLLs. Solid-state MLLs offer higher stability and lower phase noise but are typically large, heavy, and sensitive to environmental fluctuations, limiting their use mainly to laboratories. In contrast, fiber MLLs are more compact, making them easier to design, package, and use. They also have higher pumping efficiency and better heat dissipation and cooling, leading to rapid development and broad applications. Fiber MLLs are the only commercialized OFCs and provide the highest stability and lowest phase noise among the three types. For instance, Er:fiber MLLs have demonstrated absolute frequency instability at the level of $3 \cdot 10^{-18}$ at 1 s gate time. However, MLLs' output wavelengths are limited by the gain media. With advancements in micro-nano processing technology, integrated semiconductor MLLs have

made significant progress recently. These offer a small footprint, high efficiency, broad spectral coverage, and the capability for mass production. Kerr combs, the most recent addition to the OFCs family, emerged in 2007 and have become a research hotspot. Their generation relies on the small Kerr nonlinear coefficient, high quality factor (typically $Q > 10^6$), and compact size (FSR from tens of GHz to one THz) of optical resonators to enhance light–matter interaction and the Kerr nonlinear process. Kerr combs are generated based on balancing dispersion and Kerr nonlinearity, as well as parametric gain and resonator loss. They are unique among OFCs in that they can achieve an octave without nonlinear broadening, with self-referenced Kerr combs achieving instability better than 10^{-13} s^{-1}. The generation of soliton state Kerr combs usually requires fine-tuning, but recent developments have made soliton state turnkey Kerr combs possible, enhancing their role in scientific research and engineering.

E-O combs, traced back to the 1970s, were initially used for laser frequency measurement and the generation of ultra-fast, ultra-short pulses. Compared to MLLs, early E-O combs suffered from narrow bandwidth, poor stability, and high phase noise. OFCs were first used for precise time and frequency measurement, where E-O combs did not excel. However, significant breakthroughs in the past five years have revitalized E-O combs. In 2018, Carlson et al. [21] achieved octave-spanning E-O combs via nonlinear broadening, enabling the locking of f_r and f_{ceo}, resulting in a fractional stability of 310^{17} after 2000 s of averaging. In 2019, Zhang et al. [22] realized an on-chip integrated E-O comb with an 80 nm spectral width without broadening techniques, and in 2022, Hu et al. [23] increased the conversion efficiency of on-chip resonator-based E-O combs to 30% with two cascaded microrings, achieving an optical bandwidth of 132 nm. These advancements significantly improved the bandwidth, stability, phase noise, and footprint of E-O combs.

E-O combs are generated via electro-optic modulation. A CW pump laser modulated by a sinusoidal microwave signal generates sidebands on both sides of the pump frequency. This process is equivalent to cascading sum-frequency and difference-frequency generation processes of the optical pump and microwave modulation signals, with the repetition rate equal to the microwave modulation frequency.

E-O combs have several advantages. They offer a comparable or better integration level than MLLs and Kerr combs, can be based on discrete components or integrated devices, and feature a tunable repetition rate limited only by the modulation signal bandwidth. The pumping wavelength is highly flexible, and their spectra can be engineered to be very flat. However, E-O combs have a relatively narrow spectral range, which limits some applications but increases the average power per comb line, improving performance in optical communications. Despite their disadvantage in frequency stability compared to

MLLs, E-O combs are well-suited for applications not requiring high spectral stability. The phase noise amplification characteristic, although a drawback for light sources, can be exploited to generate low phase noise, tunable microwave sources. Achieving repetition rates over hundreds of GHz is challenging due to microwave source bandwidth limitations, making octave-spanning bandwidth harder to achieve compared to Kerr combs.

With OFCs evolving beyond precise frequency and time measurement, most OFC-based applications can now be realized by E-O combs. Their unique characteristics make them particularly advantageous for applications including arbitrary waveform generation, ranging, optical communications, astronomical spectrum correction, and spectrum detection.

2.2.1. Theory of E-O Combs

The generation mechanism of E-O combs relies primarily on electro-optic modulation. Currently, electro-optic modulators are predominantly based on electro-optic effects, plasma dispersion effects, or electro-absorption effects, with the electro-optic effect being the most frequently used for generating E-O combs. This effect occurs when the real part of the refractive index of the electro-optic material changes according to the amplitude of the applied electric field. The response time of the electro-optic effect can be as short as femtoseconds. Electro-optic effects include linear electro-optic effects (Pockels effect) and nonlinear electro-optic effects (secondary and higher-order electro-optic effects). The linear electro-optic effect is usually much stronger than the higher-order nonlinear electro-optic effect. Therefore, we will focus on linear electro-optic effects in this discussion. The phase modulator is the most basic component for generating E-O combs. The relationship between the input and output light of the phase modulator can be expressed as:

$$E_{out}(t) = E_{in}(t)e^{j\varphi} \tag{2.8}$$

where $E_{out}(t)$ is the output light field, φ is the phase change of the light field induced by electro-optic modulation, and $E_{in}(t)$ is the input light field, expressed as:

$$E_{in}(t) = E_0 e^{j(2\pi\nu_0 t+\varphi_0)} \tag{2.9}$$

where E_0 is the amplitude of the input light, ν_0 is the frequency of the input light, t is time, and φ_0 is the initial phase of the input light. The modulation signal is expressed as:

$$V_m(t) = V_{m0}\cos(2\pi f_{m0}t + \varphi_{m0}) \tag{2.10}$$

where V_{m0} is the amplitude of the modulation signal , f_{m0} is the frequency of the modulation signal in the RF domain, and φ_{m0} is the initial phase of the modulation signal. The phase φ is then dependent on the applied modulation voltage in the following way:

$$\varphi = \pi \frac{V_m(t)}{V_\pi} \tag{2.11}$$

where V_π is the half-wave voltage of the phase modulator, referring to the voltage required for a π-phase shift in the phase modulator. Combining Equations 2.8–2.11, we obtain:

$$\begin{aligned} E_{out}(t) = E_{in}(t) e^{j\pi \frac{V_{m0}\cos(2\pi f_{m0} t + \varphi_{m0})}{V_\pi}} = E_0 \Bigg\{ J_0 \left(\pi \frac{V_{m0}}{V_\pi} \right) \cos(2\pi \nu_0 t + \varphi_0) + \\ + \sum_{n=1}^{\infty} J_n \left(\pi \frac{V_{m0}}{V_\pi} \right) [\cos(2\pi(\nu_0 + n f_{m0})t + n\varphi_{m0} + \varphi_0) + \\ + \cos(2\pi(\nu_0 - n f_{m0})t + n\varphi_{m0} + \varphi_0) \} \end{aligned} \tag{2.12}$$

According to Eq. 2.12, the frequency interval between adjacent sidebands equals the modulation frequency f_{m0}. The amplitude of the sidebands is symmetrically distributed around the pump frequency and follows the Bessel function of different orders. The output frequency spectrum is symmetric in amplitude but asymmetric in phase. The phase of the optical carrier affects all sidebands' phases equally, while the electrical modulation signal's phase effect on the sidebands' phase is proportional to the number of sidebands. Other electro-optic modulators, such as single-drive Mach–Zehnder modulators (MZMs), dual-drive MZMs, dual MZMs, and polarization modulators (PolMs), can also generate E-O combs. They are essentially different combinations of phase modulators. In practical applications, various modulators can be combined to engineer the degrees of freedom of electro-optic modulation, resulting in E-O combs with broader and flatter spectra.

2.2.2. EOM

An electro-optic modulator operates by an electrically-induced change in the index of refraction or natural birefringence. Depending on the device configuration, it can variably control the light wave's phase, polarization, amplitude, frequency, or direction of propagation. Typically optimized for performance at a single wavelength, there is some performance degradation with wideband or multimode lasers. Electro-optic devices can be used in both analog and digital modulation formats, with the choice depending on system requirements and component characteristics (optical fibers, sources/detectors, etc.). Analog

modulation, requiring large signal-to-noise ratios (SNR), is limited to narrow-bandwidth, short-distance applications, whereas digital modulation suits large-bandwidth, medium to long-distance systems.

Device Configurations: Electro-optic modulators are classified as longitudinal or transverse, based on voltage application relative to light propagation direction. A bulk modulator generally consists of an electro-optic crystal between electrodes, modeled as a capacitor. In a longitudinal modulator, voltage is applied parallel to the light wave vector. The electrodes must be transparent or have small apertures at the crystal ends. The aspect ratio (crystal length L to electrode separation b) is always unity, and the electric field magnitude inside the crystal is E = V/L. The induced phase shift depends on voltage and light wavelength but not on device dimensions. For transverse modulators, voltage is applied perpendicular to light propagation, with the electrodes not obstructing light. The aspect ratio can be large, with the electric field magnitude E = V/b. Reducing b increases E, thus increasing the aspect ratio L/b and decreasing the voltage needed for a desired modulation degree. The interaction length can be long for a given field strength, but transverse dimension b is limited by capacitance (affecting modulation bandwidth/speed) and diffraction for a given length L, as a beam with finite cross-section diverges during propagation.

The modulation of phase, polarization, amplitude, frequency, and position of light can be implemented using an electro-optic bulk modulator with polarizers and passive birefringent elements.

2.2.3. AOM

Acousto-optic modulators (AOMs) are devices that enable modulation of the frequency, intensity, and direction of a laser beam [24]. Within these devices, incoming light Bragg diffracts off acoustic wavefronts propagating through a crystal. Modulation occurs by varying the amplitude and frequency of the acoustic waves within the crystal.

Sound waves in a crystal can be modeled as crests of increased refractive index alternating with troughs of decreased refractive index. Light incident on these refractive index gradients scatters from the acoustic wavefronts. In an AOM, the scattered light from successive wavefronts interferes constructively. Figure 2.3 illustrates two rays of light interacting with consecutive wavefronts in a crystal. Only a portion of the light is scattered from these wavefronts. The optical and acoustic wavelengths are denoted by λ_L and Λ, while θ_i and θ_d are the angles of the incident and scattered light rays with the acoustic wavefronts. The condition for constructive interference of the scattered light is given by

$$n\lambda_L = \Lambda(\sin\theta_i + \sin\theta_d) \tag{2.13}$$

where n is an integer. For an optical wave scattering from sound with a frequency of the order of 10^8 Hz, conservation of energy and momentum implies that $\theta_i = \theta_d$, approximating the equation to

$$n\lambda_L = 2\Lambda\sin\theta_d \tag{2.14}$$

The Bragg condition suggests only one deflection angle $\Theta = 2\theta_d$ is allowed, assuming acoustic and optical wavefronts are plane waves, which is an approximation. For a finite-width acoustic beam optimized for first-order maximum beam power (Bragg condition with n = 1), some light scatters at angle $m\Theta$, corresponding to other orders.

Scattering at an angle $m\Theta$ involves absorption or destruction of m phonons, whose momenta alter the light's momentum, and whose energies add to the scattered photon's energy. The change in light frequency, Δf, is

$$\Delta f = \frac{mE_{\text{phonon}}}{h} \tag{2.15}$$

where E_{phonon} is the phonon energy and h is Planck's constant. For $m < 0$, phonons are created rather than destroyed, decreasing the light's frequency. This corresponds to the reversed direction of acoustic waves in Figure 2.3.

An AOM's acoustic wave is generated by a radio frequency (RF) signal controlled by an AOM driver, comprising a Voltage Controlled Oscillator (VCO), a Voltage Variable Attenuator (VVA), and an amplifier. The VCO provides an RF sine-wave output, with the frequency determined by an applied control voltage, varying linearly with it. The VVA attenuates the VCO's output, with attenuation controlled by the VVA's control voltage. The amplifier amplifies the VVA's output to drive the AOM. The AOM's response varies with the RF signal's frequency and amplitude.

2.2.4. Single Sideband Modulator

An SSM is essentially a Mach-Zehnder Interferometer (MZI) constructed using lithium-niobate (LiNbO2) technology, where the two branches function as Mach-Zehnder Modulators (MZM) [25].
This setup is commonly referred to as a dual-parallel MZM. When an SSM is fed with

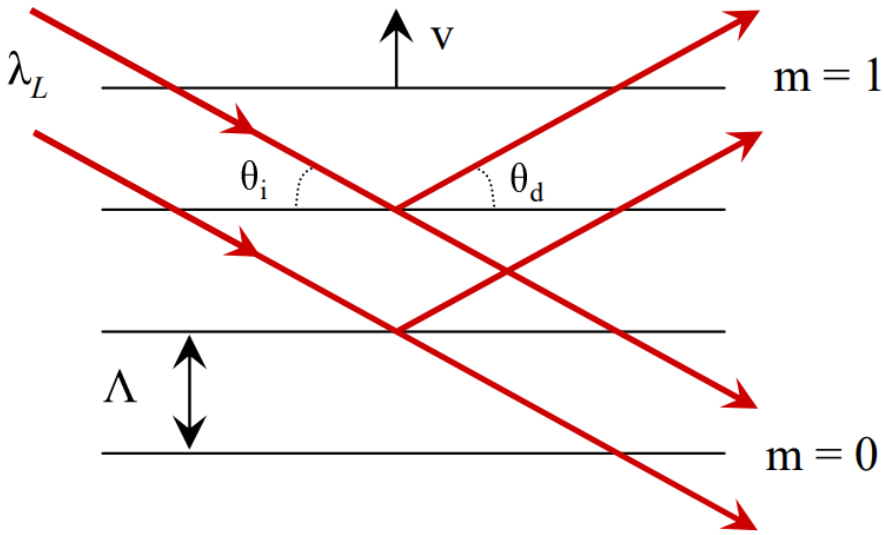

Figure 2.3: Bragg construction to identify ray directions with constructive interference.

a laser source, it produces a single broadly-tunable sideband while suppressing the input optical carrier and the other sideband, as illustrated in Figure 2.4.

In Figure 2.4, a quadrature RF signal is applied to the two branches along with suitable bias voltages to suppress the optical carrier. Suppressing one sideband relative to the other is achieved by applying a $\pi/2$ bias voltage to the outer interferometer.
High-bandwidth actuators are crucial for applications like laser-frequency control loops, where rapid frequency corrections are necessary. Typically, in a frequency control loop, a laser experiencing frequency noise is stabilized against a primary reference source such as a low-noise narrow laser or an optical resonator.
By measuring the frequency difference between the reference and the test laser, the error signal can drive the frequency actuator to correct relative frequency fluctuations between the lasers.

For actuators external to the laser source under correction, acousto-optic frequency shifters are common, where the error signal drives the acoustic wave inside the medium to correct frequency fluctuations in the first-diffracted beam. Compared to AOMs, an SSM is inherently faster, not relying on the propagation speed of the acoustic wave, enabling sub-ns response times and providing a working range of tens of GHz, much wider than that of AOMs.

When a continuous wave (CW) laser with electric field $E(t) = E_0 \cos(\omega_0 t + \varphi(t))$ is input into the SSM, it is first split equally into the two branches where static bias voltages for a π phase shift are applied. The two MZMs are driven by the RF error signal through a

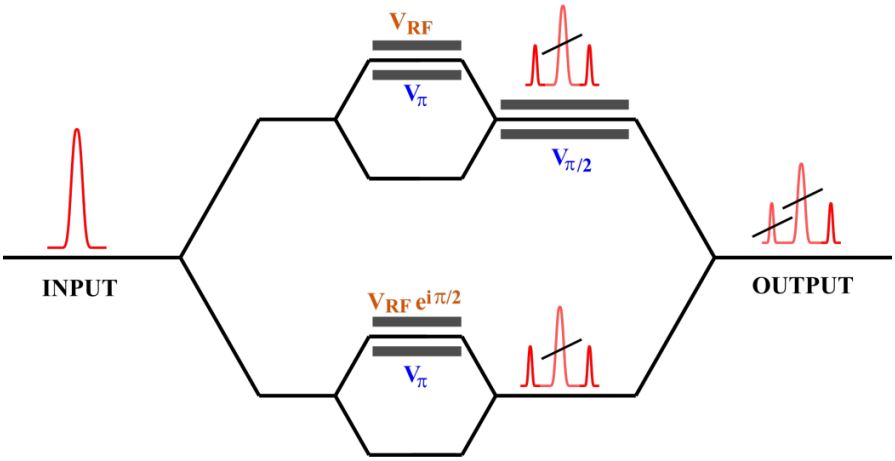

Figure 2.4: SSM con guration scheme. A quadrature RF signal is applied at the two branches together with appropriate bias voltages to suppress the optical carrier. The suppression of one sideband with respect to the other is achieved through the application of a 2 bias voltage at the outer interferometer.

90° hybrid coupler, phase-modulating the input beam branches via the Pockels effect:

$$\varphi_1(t) = G\cos(\omega_m t + \varphi_m) \tag{2.16}$$

$$\varphi_2(t) = G\cos(\omega_m t + \varphi_m + \pi/2) \tag{2.17}$$

where G is the modulation depth, ω_m and φ_m are the frequency and phase of the RF modulating signal. For the upper MZM in Figure 2.4, the input $E(t)/2$ leads to the output field expression:

$$E_1(t) = \frac{E_0}{2}\left[\cos(\omega_0 t + \varphi(t) + \pi/2 + \varphi_1(t)) + \cos(\omega_0 t + \varphi(t) - \pi/2 - \varphi_1(t))\right] \tag{2.18}$$

This simplifies to:

$$E_1(t) = -E_0\cos(\omega_0 t + \varphi(t))\sin(\varphi_1(t)) \tag{2.19}$$

where $\sin(\varphi_1(t))$ can be expressed using Bessel functions. For small modulation depths $G \ll 1$:

$$E_1(t) = -J_1(G)E_0\left[\cos(\omega_0 t + \varphi(t) - (\omega_m t + \varphi_m)) + \cos(\omega_0 t + \varphi(t) + (\omega_m t + \varphi_m))\right] \tag{2.20}$$

Similarly, for the lower MZM with a quadrature shift of the RF signal:

$$E_2(t) = -J_1(G)E_0\left[\sin(\omega_0 t + \varphi(t) - (\omega_m t + \varphi_m)) + \sin(\omega_0 t + \varphi(t) + (\omega_m t + \varphi_m))\right] 2 \tag{2.21}$$

The optical carrier is suppressed in both branches. Applying a $\pm\pi/2$ static bias voltage to the outer MZI ensures suppression of one sideband. For instance, a $-\pi/2$ phase shift leads to the SSM output field:

$$E_{\mathrm{OUT}-}(t) = 2J_1(G)E_0\cos(\omega_0 t + \varphi(t) - \omega_m t - \varphi_m + 3\pi/4) \tag{2.22}$$

This shows the (-) single sideband oscillates at $\omega_0 - \omega_m$. If ω_m reflects frequency fluctuations of a noisy laser compared to a stable reference, the SSM output sideband is a purified version of the input laser. Conversely, the (+) sideband contains twice the frequency fluctuations. Ideally, only the single sideband is present, though some spurious signals and an imperfectly suppressed carrier may remain. The single sideband contrast is typically greater than 30 dB.

One of the strengths of SSMs is their ability to tune the single sideband over more than 10 GHz without perturbing the input optical carrier. However, a challenge is providing high-RF power (+26 dBm) with a precisely fixed $\pi/2$ phase-shift over a wide frequency range, reducing the single sideband contrast if the outer MZI bias voltage is not actively controlled. This versatile modulator can serve as a frequency actuator in a Pound-Drever-Hall locking scheme, where minimizing delays in the control loop enhances the frequency locking quality, achieving MHz-level control bandwidths.

2.3. Dual Comb Spectroscopy

Dual-comb spectroscopy (DCS) merges the advantageous features of both traditional broadband spectroscopy and tunable laser spectroscopy into a unified platform [26]. Similar to conventional Fourier-transform infrared (FTIR) spectrometers, DCS allows for the interrogation of wide segments of the optical spectrum using only one photodetector. It

also shares characteristics with laser spectrometers, where the laser determines the frequency resolution and accuracy, leading to a bright single spatial mode output ideal for prolonged interrogation paths, ensuring high sensitivity.
Since its initial demonstrations, DCS has sparked significant interest, resulting in numerous proof-of-concept experiments. Over time, DCS has progressed to furnish spectra resolved down to individual comb teeth, culminating in a high signal-to-noise ratio (SNR) across broad optical bandwidths in the near-IR. Researchers have extensively explored DCS at longer wavelengths, capitalizing on strong spectroscopic signatures. Various experiments have showcased its compatibility with enhancement cavities, multipass cells, gas-filled fibers, and turbulent open-air paths. DCS has found applications ranging from ultrabroadband near-IR spectroscopy, subwavelength spatial resolution in near-field microscopy, precision metrology of molecular line centers, spectral lidar, to greenhouse gas monitoring. Moreover, it has been extended to nonlinear spectroscopy techniques like stimulated Raman scattering, comb-based coherent anti-Stokes Raman spectroscopy (CARS), and two-photon spectroscopy. As DCS continues to advance, its range of applications will inevitably expand.

At the heart of DCS lies the frequency comb laser, emitting an array of narrow, phase-coherent spectral lines or "teeth". These teeth, perfectly spaced in frequency, can all be simultaneously stabilized to an optical or radiofrequency (rf) reference. Frequency comb lasers have revolutionized various fields and have long been considered attractive sources for spectroscopy.
However, employing frequency combs for broadband spectroscopy presented challenges from the outset. To leverage the frequency accuracy and spectral resolution offered by the comb structure, each individual comb tooth must be spectrally resolved. While comb light could be coupled into conventional spectrometers, the finer comb tooth spacing compared to the resolution of most spectrometers renders the comb merely a bright, collimated light source, losing its associated frequency resolution and accuracy. Several high-resolution dispersive spectrometer and Fourier transform spectrometer techniques have been developed to fully exploit the comb structure, including virtually imaged phase array (VIPA) spectrometers, comb-cavity Vernier spectrometers, and high-resolution FTIR spectrometers. Despite compelling demonstrations of VIPA and FTIR techniques, the most widely pursued form of direct comb spectroscopy remains DCS, which eliminates the need for dispersive spectrometers entirely. This technique also appears in the literature as multi-heterodyne spectroscopy, linear optical sampling, coherent Fourier-transform spectroscopy (FTS), and terahertz (THz) asynchronous optical sampling (ASOPS), but the IR/visible community predominantly adopts the term "dual-comb spectroscopy," as used here.

DCS offers numerous advantages over conventional spectrometers in fundamental performance metrics such as frequency resolution, accuracy, acquisition speed, and SNR, as well as the potential for a compact system, as its performance isn't fundamentally limited by the optical path length of the instrument like in grating or FTIR spectrometers.

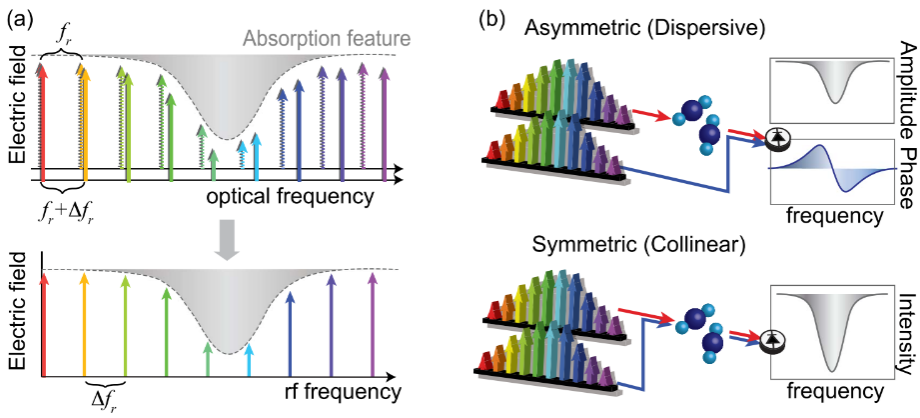

Figure 2.5: (a) Simple DCS concept. Two combs with repetition rates f_r and $f_r + \Delta f_r$ are mixed and detected by a single photo-receiver. As a result of the comb structure, each pair of optical teeth yields a RF heterodyne signal at a unique RF frequency. These radio-frequencies form an RF comb of spacing Δf_r. The RF teeth can be tightly packed such that >105 comb teeth can be observed simultaneously. For much of the original DCS work, f_r was typically $\approx$ 100 MHz and Δf_r was 100 Hz to 1 kHz, but these values could vary considerably across different frequency comb sources. (b) For spectroscopy, either one or both combs are passed through the sample. The resulting absorption (or phase shifts) on the comb teeth is encoded onto the corresponding amplitude (or phase) of the measured RF comb teeth.

The operational principle of DCS is depicted in Figure 2.5.
Two combs with slightly different repetition rates interfere on a photodiode, generating a RF comb consisting of discernible heterodyne beats between pairs of optical comb teeth. This RF comb, accessible via RF electronics, contains the pertinent spectral information from the optical comb spectra. Spectroscopy is conducted by introducing a sample into one or both optical beam paths.
The sample's response modulates the comb light, which is then detected through heterodyne detection. The specific information obtained varies depending on the system architecture, as illustrated in Figure 2.5(b).
In one configuration, one comb is transmitted through the sample and interfered with the second "local oscillator" comb, akin to the "dispersive" FTIR technique, enabling the measurement of the full phase and amplitude response of the sample. In the other sym-

metric configuration, both combs are transmitted through the sample, akin to the typical FTIR setup, measuring only the sample's absorption but offering greater robustness to turbulent measurement paths. In both cases, variations in the comb spectrum must be effectively normalized to isolate the sample's response.

To date, DCS has surpassed other comb spectroscopy techniques and swept laser spectroscopy in terms of spectral coverage, although it's unlikely to match the full spectral coverage achievable with conventional FTIR. An overview of the spectral coverage of DCS demonstrations is presented in Figure 2.6. These experiments span a wide spectrum in terms of achieved resolution, accuracy, SNR, and control of systematics, reflecting the experimental challenges associated with the unique advantages of DCS. The quality of DCS spectra largely mirrors the technological sophistication of frequency combs in the given spectral region.

The capability to simultaneously record loss and dispersion has made dual-comb approaches appealing for characterizing telecom components, fiber gratings, and microresonators. Modified dual-comb systems can monitor active sources such as static and fast-swept cw waveforms, arbitrary optical waveforms, and even pulsed or incoherent sources. These techniques share a common dual-comb/single-receiver architecture, showcasing the versatility of this approach, essentially an extension of standard heterodyne laser interferometry to frequency comb sources.

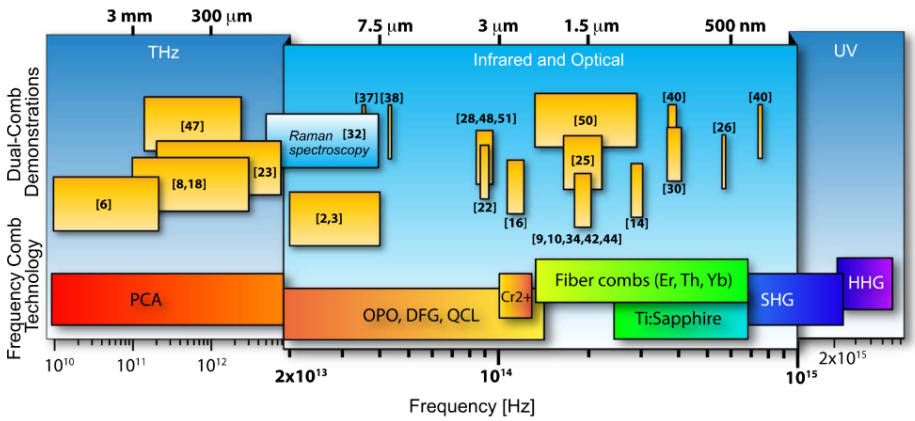

Figure 2.6: Spectral coverage of dual-comb spectroscopy demonstrations (top band) and underlying frequency comb technologies (bottom band).

2.3.1. DCS: The Ideal Case

DCS in the Time and Frequency Domains: In the frequency domain, the output of Dual-comb spectroscopy (DCS) manifests as a rfcomb, as depicted in Figure 2.7(a)

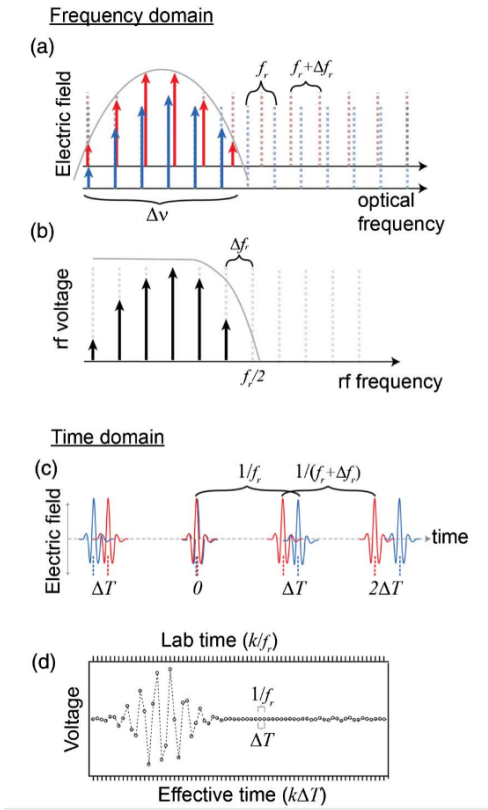

Figure 2.7: a) Two frequency combs (red and blue) are mixed to produce (b) the rf comb. Solid gray lines indicate filter functions applied in the rf and optical to avoid aliasing effects. (c) The equivalent time-domain picture showing the pulse-to-pulse walk-off between the two comb pulse trains. (d) The photoreceiver voltage output corresponds to the product of the two comb pulses, integrated over the receiver bandwidth.

and (b). The amplitude and phase of the detected rf comb teeth correspond to the product of the electric fields of the two optical comb teeth. DCS effectively transforms the optical spectrum with width $\Delta\nu$ into an rf spectrum with width $\Delta\nu/m$, where m is determined by the ratio of the comb repetition frequency, f_r, to the repetition frequency difference between the two combs, Δf_r. Compression factors typically range from 30,000 to 1,000,000, enabling the mapping of several hundred thousand comb teeth spanning tens to hundreds of THz into a 100 MHz rf band that can be digitized. The one-to-one mapping from optical to rf domain remains intact only if the optical spectral bandwidth satisfies

$$\Delta\nu \leq \frac{mf_r}{2} = \frac{f_r^2}{2\Delta f_r} \tag{2.23}$$

this condition can be doubled for in-phase/quadrature detection.

Figure 2.7(c) and (d) offer a complementary view in the time domain. Here, the two

combs sample each other with extremely fine effective time shifts between consecutive pulses, given by $\Delta T \sim \Delta f_r/(m f_r)$, falling in the picosecond to femtosecond range. This process resembles linear optical sampling or a sampling oscilloscope, where the femtosecond pulses of one comb asynchronously sample the repetitive pulse train from the other comb, resulting in a downsampled version. The resultant time-domain signal resembles an "interferogram," akin to those observed in FTIRs. The effective sampling time step per point, ΔT, imposes a Nyquist condition similar to Eq. (2.23). The time-domain perspective underscores the significance of detector linearity, as an accurate spectrum necessitates a linear detector response from the strong centerburst to the weaker tails evident in Fig. 3(d). Notably, the Fourier transform of a series of interferograms yields the rf spectrum depicted in Fig. 3(b).

To derive the sample response, one of the configurations shown in Figure 2.5(b) must be employed, with normalization by the unperturbed (i.e., sample-free) dual-comb spectrum. This yields the linear response of the sample, which can be equally well observed in either the time or frequency domain.

Acquisition Speed: The minimum time required to resolve the rf comb teeth and obtain a single spectrum is simply $1/\Delta f_r$. Consequently, there exists a direct trade-off between optical bandwidth and acquisition speed, as indicated by Eq. (2.23). Nevertheless, considering a comb tooth spacing of 100 MHz, a single spectrum encompassing over a million spectral elements can be acquired within milliseconds; narrower spectra can be obtained proportionally faster. However, this speed advantage is counterbalanced by the low signal-to-noise ratio (SNR) per single spectral acquisition. In practical scenarios, multiple spectra need to be co-added, and the minimum acquisition time is determined instead by the required SNR. Nonetheless, the rapid single-shot acquisition proves crucial for measurements in turbulent environments, as turbulence-induced noise becomes "frozen" out over a single interferogram. Additionally, the advancement of mid-IR and far-IR DCS, along with extended interaction path lengths through optical cavities, multipass cells, and open paths, may alleviate the demand for high SNR to some extent by offering enhanced absorption signals. It's worth noting that this speed increases with the square of the comb tooth spacing. Emerging technologies like microresonator combs, electro-optic modulator (EOM) combs, and quantum cascade laser (QCL) combs with repetition rates surpassing 10 GHz could potentially facilitate recording complete spectra within time scales below 1μs. While the spectral spacing may be relatively coarse, such devices hold promise for studying fast dynamic processes such as chemical reactions or swiftly measuring the broad absorption features of liquids or solids.

It's important to note that the aforementioned discussion assumes the digitization of an

entire interferogram. However, in practice, only a limited region around the centerburst of the interferogram can be digitized, resembling an apodized interferogram in conventional Fourier-transform spectroscopy (FTS) terminology. This apodization nominally reduces the acquisition time of a specific single spectrum, although the acquisition rate of consecutive spectra remains Δf_r. Furthermore, the frequency comb structure is lost due to the Fourier transform of the apodized interferogram yielding a spectrum smoothed across comb teeth. While this spectral smoothing improves the SNR per (coarser) spectral point at the expense of lower spectral resolution, the SNR for detecting a particular molecular species remains unchanged, as it remains independent of the spectral smoothing.

Signal-to-Noise Ratio: One advantage of DCS lies in its requirement for only a single detector to capture millions of spectral points. However, employing a single detector incurs a "multiplexed" penalty. Essentially, for M spectral elements (i.e., comb teeth), the signal-to-noise ratio (SNR) per spectral element is expected to scale as $1/\sqrt{M}$ as the fixed laser power is distributed over M spectral elements. Nonetheless, utilizing a single detector introduces an additional penalty, resulting in an overall SNR scaling with 1/M. In the ideal scenario of shot-noise limit, the SNR is approximately $\sqrt{(\tau * n_{comb}/M)}$, where τ represents the acquisition time and n_{comb} denotes the number of detected comb photons per second. However, the actual SNR per spectral element varies depending on the dominant noise source. Nevertheless, the fundamental scaling law of SNR $\approx \sqrt{(\tau/M)}$ persists, illustrating the trade-off between SNR and bandwidth, given that $\Delta v \propto M * f_r$. This underscores the significance of a lengthy coherent averaging time, or equivalently, a prolonged effective mutual coherence time between combs, which determines the maximum achievable τ.

2.3.2. DCS With Imperfect Combs

The previous section presented an idealized view assuming perfect frequency combs comprising narrow, delta-function-like comb teeth at precise frequencies. While actual frequency combs can approach this ideal performance, achieving it experimentally poses challenges. DCS intensifies these challenges by necessitating two such combs with high mutual coherence. In practice, DCS has been demonstrated across a broad spectrum of frequency comb performance. Broadly, DCS demonstrations fall into three categories: free-running combs, mutually coherent combs, and fully referenced combs, as depicted in Figure 3.6(a) and summarized below. The experimental hurdles increase progressively from free-running combs to fully referenced combs, but so does the performance in terms of enhanced spectral resolution, frequency accuracy, and SNR (through extended coherent averaging times).

Figure 3.6(a) illustrates the scenario of free-running combs, where the relative optical linewidth between the combs exceeds Δf_r. Consequently, there may be varying degrees of overlap or blending with the corresponding rf comb, resulting in significantly lower frequency resolution. Nonetheless, demonstrations with free-running combs have played a crucial role as fundamental proof-of-concept experiments, including the pioneering demonstration of DCS by Keilmann and colleagues, cavity-enhanced DCS, and numerous demonstrations with innovative comb sources in the mid-IR and far-IR.

Figure 3.6(b) portrays the scenario of high mutual coherence, where the relative linewidth between the combs is well below Δf_r. Mutual coherence can be enforced through active feedback mechanisms or signal processing, as discussed later, or through comb designs where coherence is at least partially intrinsic. In this scenario, individual comb teeth are spectrally resolved, providing independent spectral samples. Due to the narrow linewidth of comb teeth, there is minimal cross talk between adjacent spectral elements, distinguishing DCS from conventional broadband spectrometers with inherent instrument line shapes. Moreover, the spectral point spacings typically match the highest resolution FTIRs, serving as the benchmark for high-resolution broadband spectroscopy. Additionally, high mutual coherence allows for extended acquisition times and higher SNR.

Lastly, Figure 3.6 represents the "ideal" scenario, where the two mutually coherent combs are referenced to an absolute frequency standard. This is more straightforward with combs based on difference frequency generation (DFG) or THz combs, where the carrier-envelope offset frequency f_{ceo} is zero. Even in cases where f_{ceo} is not zero, stabilizing it enables comb teeth to achieve kilohertz accuracies, surpassing the accuracy of conventional broadband spectrometers by orders of magnitude. Absolute referencing also mitigates common-mode frequency drifts between the combs, preventing broadening of the instrument line shape over extended averaging times and preserving spectral features. Molecular line centers retrieved with fully stabilized DCS exhibit superior frequency accuracies compared to high-resolution FTIRs and are traceable to the underlying frequency reference. However, spectral distortions may limit line center retrievals to about a part per thousand of the linewidth.

2.3.3. Dual Path EO-DCS

In dual path configurations, DCS can significantly enhance the detection capabilities by utilizing two distinct optical paths for the probe and local oscillator (LO) signals [27]. This approach not only improves the SNR but also allows for precise and rapid measurements, making it ideal for various applications in gas analysis, metrology, and other scientific

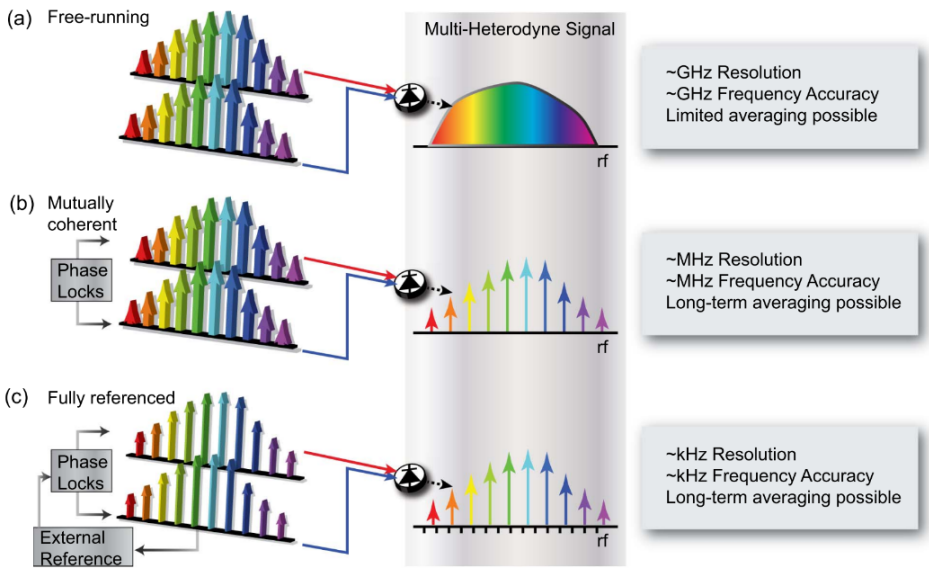

Figure 2.8: Three different categories of DCS demonstrations. (a) Free-running combs can yield dual-comb spectra, but with low resolution, low frequency accuracy, and low SNR, since only limited signal averaging is possible; (b) mutually coherent combs can yield comb-tooth-resolved spectra that can be averaged for high SNR; and (c) fully referenced combs yield spectra with simultaneous high resolution, absolute frequency accuracy, and high SNR. Text boxes indicate some general rules of thumb for frequency combs based on mode-locked lasers.

fields.

To optimize bandwidth requirements for detection, multiheterodyne spectroscopy typically utilizes two OFCs with slightly different comb spacings. One of these OFCs probes the gas sample of interest, whereas the other serves as a LO. The two OFCs are then combined on a photodiode for bandwidth compression and detection in the RF domain. Each optical frequency component of the probe laser exhibits a unique RF beat frequency with the LO in the heterodyne signal, thus allowing for the entire OFC to be simultaneously recorded with a spectrum analyzer. Importantly, this method requires no mechanical motion (unlike Fourier-transform spectroscopy, which uses a moving mirror) and therefore allows for high-speed measurements.

A schematic of a dual path EO-DCS can be found in Figure 2.9. The OFCs are generated using dual-drive Mach–Zehnder modulators. The use of dual-drive MZMs allows for power leveling of the resultant OFC by attenuation of one of the two drives and control of the phase condition through the use of an external DC bias. Two OFCs (a probe and LO) whose comb spacings differs by δf_{mod} are produced from a single external-cavity diode

laser using the two MZMs. In addition, a fiber-coupled acousto-optic modulator (AOM) is used to shift one of the OFCs. This moves the heterodyne signal away from DC, thus reducing the effects of $1/f$ noise, and ensures that each pair of optical frequency components corresponds to a unique RF frequency.

In order to normalize the probe-LO heterodyne signal, a reference OFC can be added that does not interact with the gas sample. Driving the probe and reference comb AOMs at slightly different frequencies produces two interleaved heterodyne signals. The frequency spectrum corresponds to the magnitude of the Fourier-transformed time-domain signal. The ratio of the nth pair of frequency components yields the normalized transmission signal at the probe frequency, $f_{n,Probe}$. This is a complex quantity containing phase and amplitude information. The magnitude of this transmission signal is proportional to the field amplitude of the probe laser after passing through the absorbing sample, and therefore equals the square root of the transmission signal normally measured as a ratio of intensities. The phase of the heterodyne signal is also sensitive to the dispersive phase shift of the probe beam, which is caused by propagation through the absorbing medium.

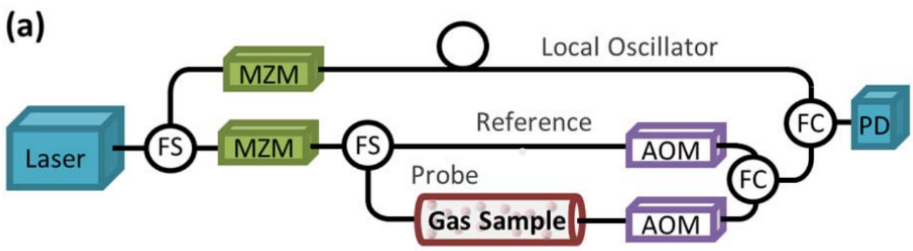

Figure 2.9: Schematic of the multiheterodyne spectrometer. FS and FC denote fiber splitters and fiber combiners.

2.3.4. Single Path EO-DCS

Dual comb spectroscopy (DCS) can be implemented in both single path and dual path configurations. In a single path setup, a single optical path is used for both the probe and local oscillator (LO) signals, which simplifies the system but may introduce certain limitations [28]. On the other hand, dual path DCS utilizes separate optical paths for the probe and LO signals, enhancing signal processing capabilities and reducing noise. This distinction impacts the complexity, stability, and sensitivity of the measurements, with dual path setups generally providing better performance in terms of signal-to-noise ratio (SNR) and resolution.

A method to generate a single-path dual-comb uses a single electro-optic modulator, fed

by a low phase noise continuous-wave (CW) laser, and driven by an arbitrary waveform generator (AWG). This setup produces an optical spectrum composed of two interleaved frequency combs with slightly different line spacings. Each comb line forms a periodically repeated doublet with a frequency difference that increases linearly across the optical bandwidth. This configuration allows for spectroscopic analysis with a simplified one-arm setup, using only one photodetector instead of a high-resolution spectrometer.

The spectral fingerprinting of the sample is encoded onto low-frequency beat notes, created by the interference of the closest neighboring lines of the dual-comb spectrum. The common-path architecture of this dual-comb interferometer allows for self-referenced measurements without the need for real-time correction methods or feedback loops. The system's stability enables integration times close to 1 second, significantly enhancing the SNR across averaged interferograms. The AWG technology employed can resolve extremely sharp optical features, down to the order of MHz or below.

The operation principle involves a CW laser modulated by a modulator driven by a signal from an AWG. This signal includes information for both combs, with line spacings of Δf and $\Delta f + \delta f$, respectively. The modulator is biased to suppress the optical carrier, producing two symmetric sidebands. One sideband and the residual carrier are filtered out using a tunable optical bandpass filter (TBPF). The remaining light passes through the sample and is detected by a photodiode. The electrical signal, after spectral analysis, maps the optical spectrum into the electrical domain, with the RF comb line spacing equal to δf, creating a compression factor (CF) of $\Delta f/\delta f$. This downconversion is unambiguous due to the TBPF, which removes beat notes from the other optical sideband.

The method's common-path configuration eliminates uncorrelated optical phase fluctuations between the combs, providing enhanced stability. The spectral response of the sample is encoded onto the dual optical frequency comb, with the electrical amplitude response corresponding to the square of the optical amplitude response. This setup offers double optical amplitude sensitivity compared to configurations where only one comb interacts with the sample.

3 | Experimental Setup

In this thesis work, we propose a method to generate a single path dual-comb using a single electro-optic modulator, driven by an arbitrary waveform generator (AWG), starting from an ultra-low noise single mode CW laser. This approach produces an optical spectrum composed of two interleaved frequency combs with a small offset in their line spacing. This spectrum appears as a sequence of periodically repeated doublets, each consisting of two lines whose frequency difference increases linearly along the optical bandwidth. The resulting dual-comb generator allows for spectroscopic interrogation with a simplified one-arm setup, including only one photodetector instead of a high-resolution spectrometer. The spectral fingerprint of the sample is encoded onto low-frequency RF beat notes, created by the interference of the closest neighboring lines (doublet lines) of the optical dual-comb spectrum.

3.1. Spectrometer Layout

The setup incorporates a free-space section dedicated to the gas chamber and a fully-fibered common-path arrangement that results to be fundamental to the compactness of the whole spectrometer. It is worth to highlight that the spectrometer has been carefully designed to reduce as much as possible the footprint. As it has been described earlier, this spectrometer should constitute a facility that can be applied to several different fields and should allow to perform *in situ* measurements. This is why it has been mounted on a cart equipped with wheels. This mobile cart will provide several practical benefits, including:

- **Mobility:** the mobile setup allows the spectrometer to be easily moved to different environments, whether it's within the same laboratory or to other locations for field measurements or collaborative projects;
- **Stability:** despite its mobility, the cart has been designed to offer a stable and secure platform for the spectrometer, ensuring that measurements are minimally affected by vibrations during operation;
- **Accessibility:** the cart has been designed at an ergonomic height, creating a suit-

able place for keyboard and mouse and accommodating the PC under the spectrometer. This ensures that the spectrometer's configuration and the data collection can be performed comfortably and efficiently;

- **Expandability:** the cart can be equipped with additional shelves or compartments to upgrade or modify the system with optical or mechanical components, electronics or data acquisition systems needed for specific applications.

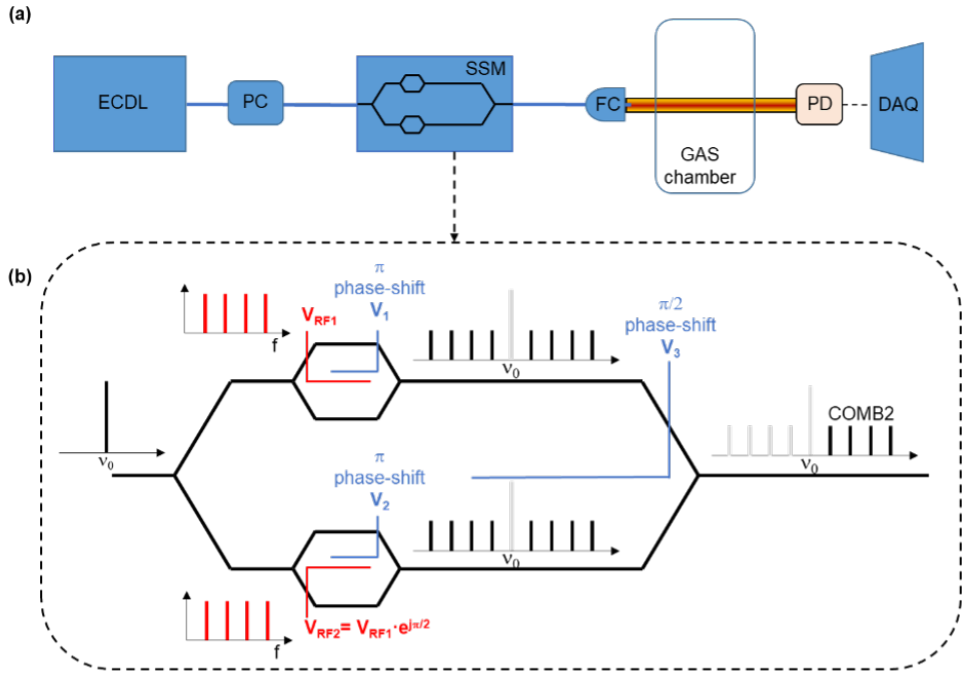

Figure 3.1: Experimental setup of the EO dual comb spectrometer

The layout of the spectrometer is illustrated in Fig. 3.1 (a). The spectrometer is based on a fiber-coupled extended cavity diode laser (ULN15TK) operating at $\lambda_0 = 1550$ nm, which is followed by a polarization controller seeding a single sideband modulator (SSM) with a bandwidth exceeding 40 GHz. Typically employed as an external modulator in fiber communication systems for implementing quadrature phase shift keying (QPSK), this SSM is used to generate a single set of sidebands on each polarization state across a 25 GHz span ($\simeq 1$ cm^{-1}). This range is limited by the maximum bandwidth of the arbitrary waveform generator (AWG, Keysight M8195A).

The RF signal provided to the AWG, designed offline as detailed in subsection 3.3, allows to generate both combs with line spacing f_{r_1} and $f_{r_2} = f_{r_1} + \Delta f_r$, respectively, with $\Delta f_r << f_{r_1}$. The signal is then loaded into the AWG which produces the wavefunction that modulates the single sideband modulator.
This setup differs from conventional schemes, which combine signals in the optical domain

and are subject to uncorrelated optical phase fluctuations between the combs. The SSM biases are adjusted to suppress the optical carrier, yielding only one sideband.

The light emerging from the optical filter is sent to the sample under test and detected by a single photodiode. Spectral analysis of the measured electrical signal (filtered and amplified as necessary) maps the optical spectrum into the electrical domain. In the lowest RF region, the interference between the nearest neighboring lines of the dual-comb structure produces an electrical RF comb with a line spacing equal to Δf. The downconversion is unambiguous because the SSB cancels out one of the sidebands and the carrier. The spectral response of the sample is encoded onto the dual optical frequency comb, and the spectral amplitude response can be easily retrieved. The electrical amplitude response encoded in the beat of each doublet corresponds to the square of the optical amplitude response of the sample, providing double optical amplitude sensitivity compared to a setup where only one of the two combs interacts with the sample. The innovative suppression of one set of sidebands is a crucial feature of our spectrometer design. By eliminating the aliasing between left and right sidebands, which is a common issue rising inconventional phase modulators, our approach ensures cleaner and more accurate spectral measurements.
This design also eliminates the need for an acousto-optic modulator to offset the two combs, a component necessary in recent implementations of electro-optic dual-comb spectroscopy (EO-DCS). The removal of this component simplifies the setup, reducing potential points of failure and enhancing the overall robustness of the system.

Furthermore, this configuration enhances the spectrometer's performance in harsh environments. The simplified design, with fewer components that can drift or degrade over time, maintains mutual comb coherence for durations up to 1 second without phase correction. This level of stability and reliability is critical for applications where consistent and long-term operation is necessary, such as in field measurements or industrial environments.

For detection and acquisition, we will synchronize all microwave sources to a common clock. This synchronization is essential to ensure that the difference between the spacing of the two combs (Δf_r) is an integer multiple of the spacing themselves (f_{r_1} and f_{r_2}). This choice results in an integer number of points per interferogram facilitating the real-time co-addition and averaging of the interferograms before they undergo Fourier transformation.

3.2. Low Noise Single Mode Laser

Thorlabs' ULN15TK is a turnkey, ultra-low-noise (ULN) single mode laser system. It incorporates Thorlabs' ULN15PC component in an extended butterfly package, combined with a low-noise driver and temperature stabilization system within a benchtop housing. The driver electronics are optimized to minimize current noise, ensuring the specified narrow linewidth of the ULN15PC laser. The drive electronics also feature two temperature stabilization circuits for both the laser chip and the Fiber Bragg Grating (FBG). Additionally, the laser case temperature is stabilized by a third temperature stabilization circuit, providing long-term power and wavelength stability in standard laboratory environments. A fiber isolator is included at the laser output to reduce the impact of back-reflected light. The main feature of such a laser is related to the very narrow linewidth that in our case is at the level of 80 Hz, as it can be retrieved from the frequency noise measurement provided by Thorlabs (Figure 3.2 and Figure 3.3). The laser presents a relative intensity noise (RIN) of -160 dBc/Hz.

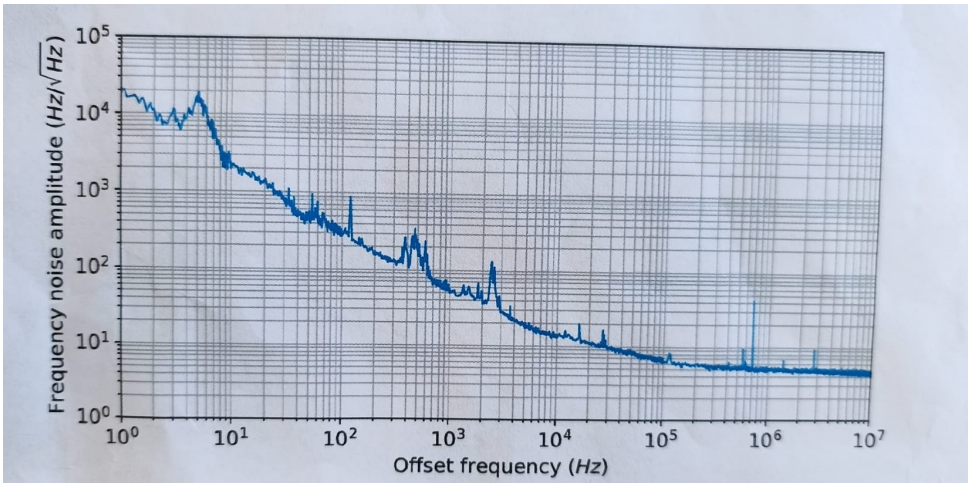

Figure 3.2: Laser frequency noise.

3.3. Arbitrary Waveform Generator

The Keysight M8195A is a 65 GSa/s Arbitrary Waveform Generator able to generate any mathematically defined waveform, ultra-short yet precise pulses and extremely wideband chirps with an analog bandwidth of 25GHz. The optimized design of the electrical signal driving the SSM is achieved through digital synthesis in the frequency domain whose preliminary step has been performed in the Matlab environment that is directly compatible with the instrument. The process begins with the numerical synthesis of two individual frequency combs on a computer, with line spacings of f_{r_1} and f_{r_2}. The frequencies con-

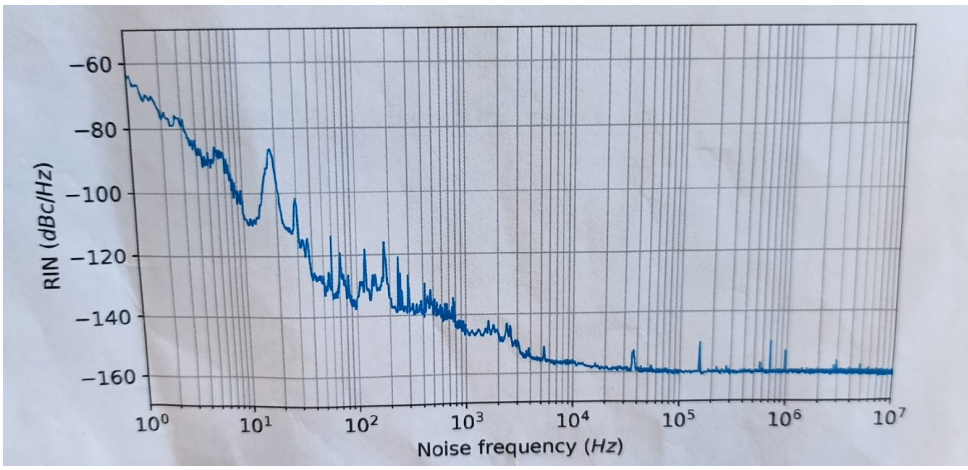

Figure 3.3: Laser RIN.

stituting the two combs are selected based on the design parameters such as the number of comb modes, the optical bandwidth, and the frequency offset. These parameters are subject to constraints which are detailed in the following subsection 3.4 . Once the comb frequencies are defined, a random phase is allocated to each spectral line to avoid the formation of high peak-power pulses, which can easily saturate the modulator driver and the photodetector. To recover a real-valued signal at the end of the design process, the spectrum of each comb must be conjugated symmetrically around $f = 0$.

After numerically constructing the individual combs, they are added in the digital domain to form a single complex spectrum. Mathematically, the designed spectrum can be defined by the expression:

$$\begin{aligned} E(f) = &\sum_{m=0}^{N-1} A_m[e^{j\phi_m}\delta(f - f_m) + e^{-j\phi_m}\delta(f + f_m)] + \\ &+ \sum_{m=0}^{N-1} A_m[e^{j\phi_m}\delta(f - f'_m) + e^{-j\phi_m}\delta(f + f'_m) \end{aligned} \tag{3.1}$$

where A_m, f_m, and ϕ_m are the amplitude, frequency, and random phase value of the mth comb line respectively. The frequency of each line can be decomposed in terms of the line spacing:

$$f_m = f_s + mf_r \tag{3.2}$$

$$f'_m = f'_s + m(f_r + \Delta f_r) \tag{3.3}$$

where f_s defines the frequency of the first line of one comb ($m = 0$). The first line of the second comb is set at $f'_s = f_s + \Delta f_r$, allowing the first line of the downconverted comb to be evaluated. The time-domain representation of the modulating signal is obtained through an inverse Fourier transformation, i.e., $E(t) = \mathcal{F}^{-1}E(f)$. In the temporal domain, e(t) corresponds to a summation of cosines, each with identical amplitude and frequency f_m, and different phase values.
From an implementation perspective, designing the DFCs in the spectral domain proved to be computationally more efficient. This digital signal $E(t)$ is uploaded to the AWG to ultimately generate the electrical signal driving the SSM.

3.4. Single Sideband Modulator

The modulator selected to design the single path dual comb spectrometer is the Lumentum CDM0010AC, shown in Fig. 3.4. This device is an integrated coherent driver modulator, which features a four-channel modulator driver integrated circuit co-packaged with two nested modulators, designed to modulate the amplitude and the phase of the input light in both polarizations. The control of the modulators is made via analog voltage inputs to the module. The control of the driver is via SPI digital control interface along with analog control signals. The device features monitoring photodiodes to detect power and provide feedback for control loops.
The module has one polarization maintaining input fiber and one output fiber. Forty low speed contacts located at the side of the package provide power supply, control signals, and the digital SPI interface. Electrical interfaces are provided through the 40-pin connector.
The module contains a high-speed quad-channel modulator driver, controlled via an SPI interface and equipped with circuitry for gain control and RF peak detection. The driver is connected to a nested modulator, with bias contacts managed by external electrodes. The temperature of the InP modulators is regulated by a thermo-electric cooler. Inside the package, a set of photodiodes provides power monitoring and a control feedback. The MZ structures incorporate SOAs (semiconductor optical amplifiers) that can be used to reduce insertion loss or to balance power in both polarizations. The SOAs are current-controlled, with two per polarization located before and after the MZM. To drive them we use PLD12.5K-CH which ensures great reliability and is described in detail in section 3.4.4.
As stated before, the modulator has the ability to modulate the signal in both polarizations, however for our current application we will not use this feature since it is not needed, yet it is important to highlight that this capacity opens up the possibility for

future developments of the set-up.
The modulator has a bandwidth of 35GHz at -3dB and of 42GHz at -6dB, both higher than the 25GHz bandwidth of the AWG which is therefore the bottleneck. To exploit the whole 25GHz bandwidth it is necessary a particular cable.To stabilize the temperature of the Single Sideband Modulator we used the Alpes Laser TC-3.

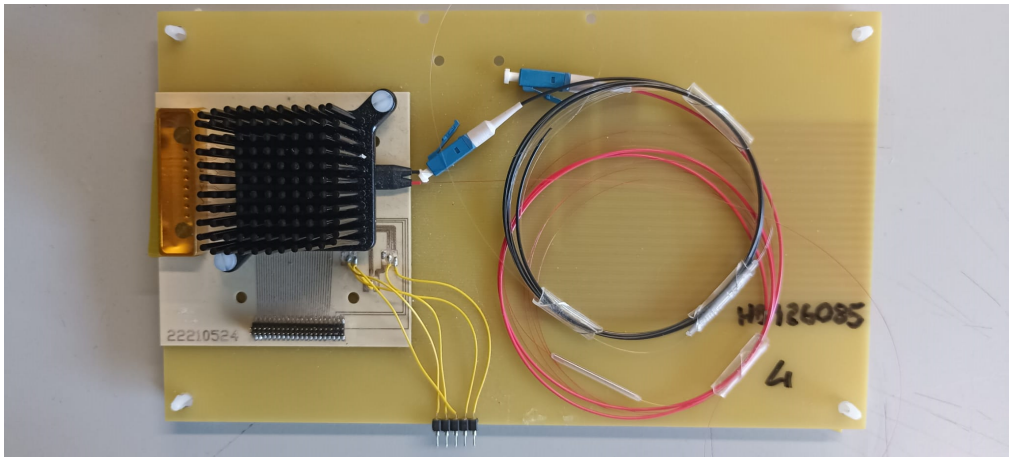

Figure 3.4: Modulator Lumentum CDM0010AC

3.4.1. MXPM90 Cable

Huber Suhner MXPM90 is a broadband low-loss cable with an operating range at up to 90GHz, way above our necessities. The innovative design allows ultra-precise and highly repeatable S-parameter measurements up to 90 GHz with minimal impedance variation at the PCB transition. The broadband return loss and insertion loss characteristics over the entire bandwidth, along with the tight phase matching of the single assemblies, guarantee best-in-class signal integrity for data analysis up to 112 Gbps and beyond. The ultra-compact design, with its 2.54 mm pitch center-to-center, places MXPM as close as possible to the DUT/chip to keep traces short and losses low. The integrated magnetic locking mechanism prevents inappropriately mated counterparts and ensures the electrical connecting reference is defined as precisely as possible at any time.

3.4.2. Alpes Laser TC-3

We chose Alpes Laser TC-3 for the temperature control in the testing phase due to its great reliability and ease of use.
TC-3 combines leading edge technology with years of experience in temperature control.

Featuring a crystal clear VFD display, high power outputs, multi-sensor support, RS232

Figure 3.5: Alpes Lasers TC-3 during the control of the modulator temperature.

and USB computer interfaces, and a compact design, the TC-3 is suitable for almost any temperature control application.

Unlike other controllers in its class that use inexpensive 7-segment LED displays, the TC-3's large VFD display simultaneously shows set point temperature, actual temperature, current, and voltage.

The user interface of the TC-3 is designed for simplicity. With text-based menus, there is no confusion over which setting is being changed, and parameters are displayed in clear English, avoiding cryptic numbers or LEDs.

The TC-3 includes features expected from a modern temperature controller: - AutoTune for automatic PID parameter calculation - 0.004°C temperature stability - 0.01°C resolution for both set point and actual temperatures - 60W (5A/12V) and 120W (10A/12V) output power

The biggest disadvantage of this temperature controller lies in the size, which is not a problem in the testing phase but is not optimal for the definitive setup. For this reason we plan to substitute it with a more compact device, the WTC 32ND, which can be implemented directly on the board, guaranteeing a far greater handiness, portability and versatility for the setup.

3.4.3. WTC 32ND

The WTC32ND is a compact, analog PI (Proportional, Integral) control loop circuit optimized for use in ultrastable thermoelectric temperature control applications. It easily handles variable operating conditions with a stability of better than 0.0009ºC. The temperature setpoint is set by a remote voltage signal. It is capable of controlling both

thermoelectric and resistive heaters, and only five external resistors are needed to optimize the controller for your specific application. The WTC32ND-EV Evaluation Board is available to quickly integrate the WTC32ND into your system and can be optimized for sensor type.
It's main features are:
• Linear PI Control Stability of 0.0009°C
• Heat and Cool Current Limits
• Adjustable Sensor Bias Current
• Drive ±2.2 A of TEC or Resistive Heater Current
• Small Size of 1.3" X 1.28" X 0.313"
• Supports Thermistors, RTDs, and IC Sensors
• Single Supply Operation: +5 V to +30 V
• 14-pin DIP PCB Mount
• Monitor Actual Temperature

As already said, the most important for our purpose is the reduced size which permits us to directly install it on the board described subsequently.

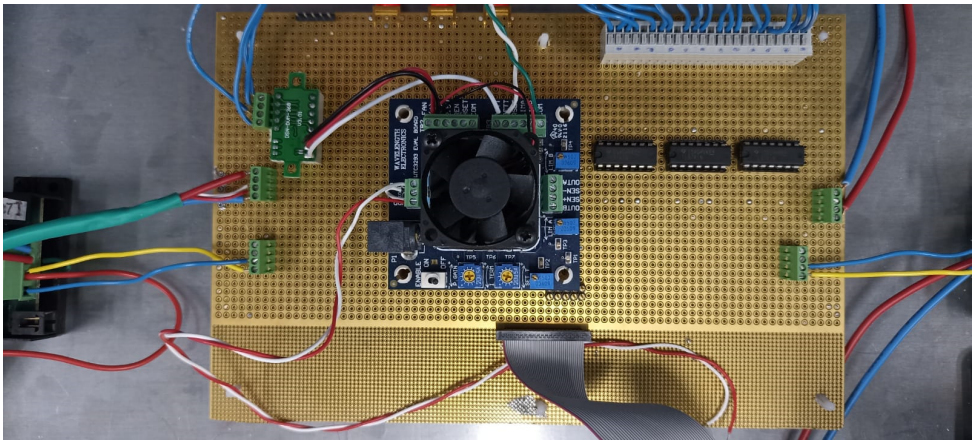

Figure 3.6: WTC3293

3.4.4. PLD12.5K-CH

The PLD12.5K-CH Laser Diode Driver offers great reliability and performance housed in a compact, easy-to-integrate chassis-mount package. It is utilized in various applications including industrial cutting and welding, manufacturing vision systems, photovoltaic quantum efficiency testers, fiber aligners, and laser diode LIV testers. The PLD12.5K-CH requires separate power supplies for the driver and the laser, allowing you to select the

best low-noise, high-power supplies for your application.
Built-in features enhance robustness and reduce electronics overhead:
• Remote enable can be connected to a safety interlock and a temperature controller, such as Wavelength's PTC Series.
• Built-in Constant Current and Constant Power operating modes reduce electronics overhead.
• Analog setpoint input allows remote external control of laser current and modulation.
• Latching current limit safely switches off output if the current limit is reached.

The PLD12.5K-CH has an output current of 12.5A, way above our required currents of 150mA for the Pre SOA and 200mA for the Post SOA. Another great feature lies in its possibility to be driven with grounded cathode, which is required by the SOAs.

3.5. Board

To ensure a correct communication between the different elements of the set-up we designed the breadboard shown in Figure 3.7.
The connector with 40 pins on the left is connected to the Single Sideband Modulator:
12 of the 40 pins of the connector take the voltages from the PCIe described in section 3.6 and give them to the various phases of the Single Sideband Modulator.
To drive the phases there are some buffers in between since the modulator needs currents.
Every buffer has a positive voltage at its positive input, the negative input is connected to the output.
The different grounds of the PCIe are short-circuited and connected to the ground of the 40 pin connector, and so to the ground of the modulator.
We used three TL974IN by Texas Instruments, better described in the next subsection, for their low noise and high output current.
We have actually used only 6 of the 12 voltages since, for now, we needed to pilot only half of the modulator (the upper part relative to only one polarization).
To alimentate the operational amplifiers we used an Agilent E3630A, suitable for the testing phase for its reliability and easy use.

4 of the 40 pins of the connector take the currents from the laser's drivers which are more stable and give them to the Pre and Post-SOAs. Again, as before, we utilized only two of the four SOAs.

4 of the 40 pins of the connector are connected to Vcc, Vdr, Vsub and GND that are

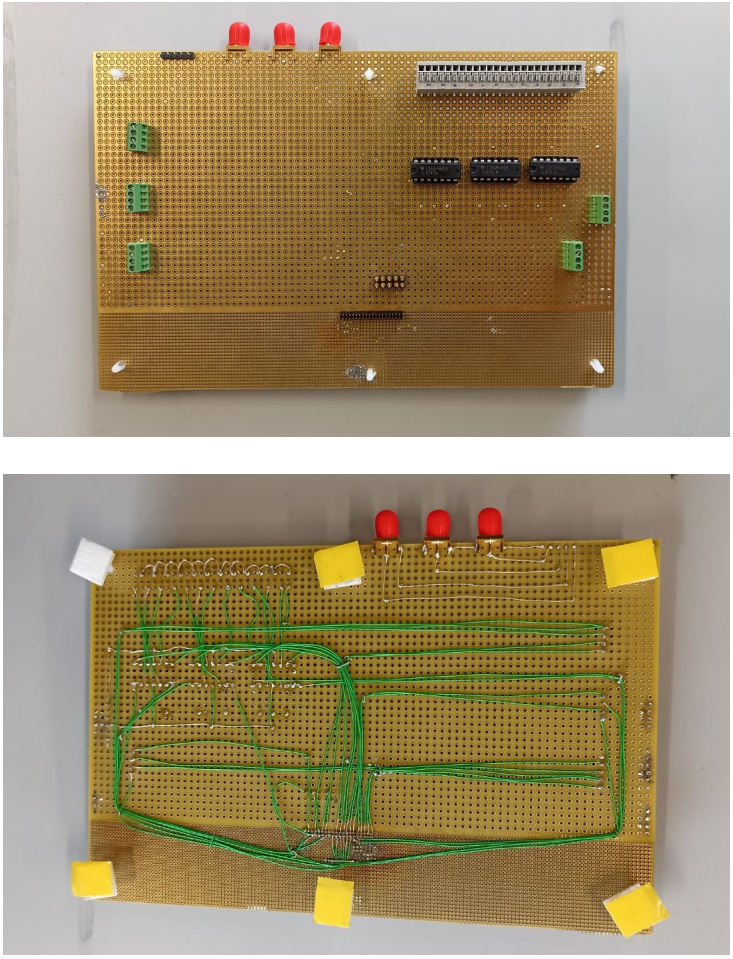

Figure 3.7: Breadboard

the voltages of the electronics and of the substrate. These voltages come from the PCIe 6738.

2 of the 40 pins of the connector are connected to the thermistor from which we take the signal that is used to stabilize the temperature through the TEC. The TEC is connected to 2 other pins of the same connector.

3 of the 40 pins of the connector are used for the USB-SPI connection. We didn't exploit it yet, but it will be useful in the future to regulate some device parameters.

In the upper right part of the board there are the connections of the monitoring photodiodes.

The board shown in Figure 3.7 will be substituted by a more professional, non hand-

made, board which will be more reliable and compact. This board has been useful for the testing phase to develope the best possible configuration for the setup; all its small defects will be corrected in the definitive version.

3.5.1. TL974IN

The TL972IN operational amplifier operates at voltages as low as ±1.35 V and features an output rail-to-rail signal swing with VCC = ±2.5 V. These amplifiers offer a very low noise level of 4 nV/Hz, ultra-low distortion of 0.003% and high dynamic features including a 12 MHz bandwidth and a 5 V/s slew rate. The TL972IN is particularly well-suited for portable and battery-powered equipment, making it ideal for applications requiring very low noise and low distortion.

3.6. PCIe 6738

To guarantee the correct use of the modulator, it is necessary to give the various voltages respecting the time schedule shown in Fig.4.8. To this purpose, we used PCIe 6738 of National Instruments. The PCIe-6738 is a high-speed, high-density analog output device designed to deliver simultaneous, multichannel updates for control and waveform output applications. In addition, the device provides eight 5 V TTL/CMOS digital I/O lines, two 24-bit, 20 MHz counter/timers and digital triggering and external clocking capabilities. To manage all the different tensions and their timing we used a LabView code appositely developed. During the testing phase we connected the PCIe to the board using a terminal block for its versatility. In the definitive set-up the connection will be via a connector.

3.6.1. LabView Code

The code shown in Figure 3.8 communicates with the PCIe-6738 and allows us to generate the desired tensions with the desired timing.
To communicate with the PCIe we used the dedicated functions of the NI DAQmx packet: DAQmx Create Channel to connect with the DAQ and to select the channels relative to the outputs we want to use, DAQmx Start to open a task in which we will set the voltage of one or more outputs, DAQmx Write to set the voltages, DAQmx Stop to close the task and DAQmx Reset to put all the voltages to zero at the beginning and at the end of the code.
The first operation of the code is made by the DAQmx Reset block which puts all the voltages to zero, then, inside of the "Single Output" sub VI, a connection with the PCIe

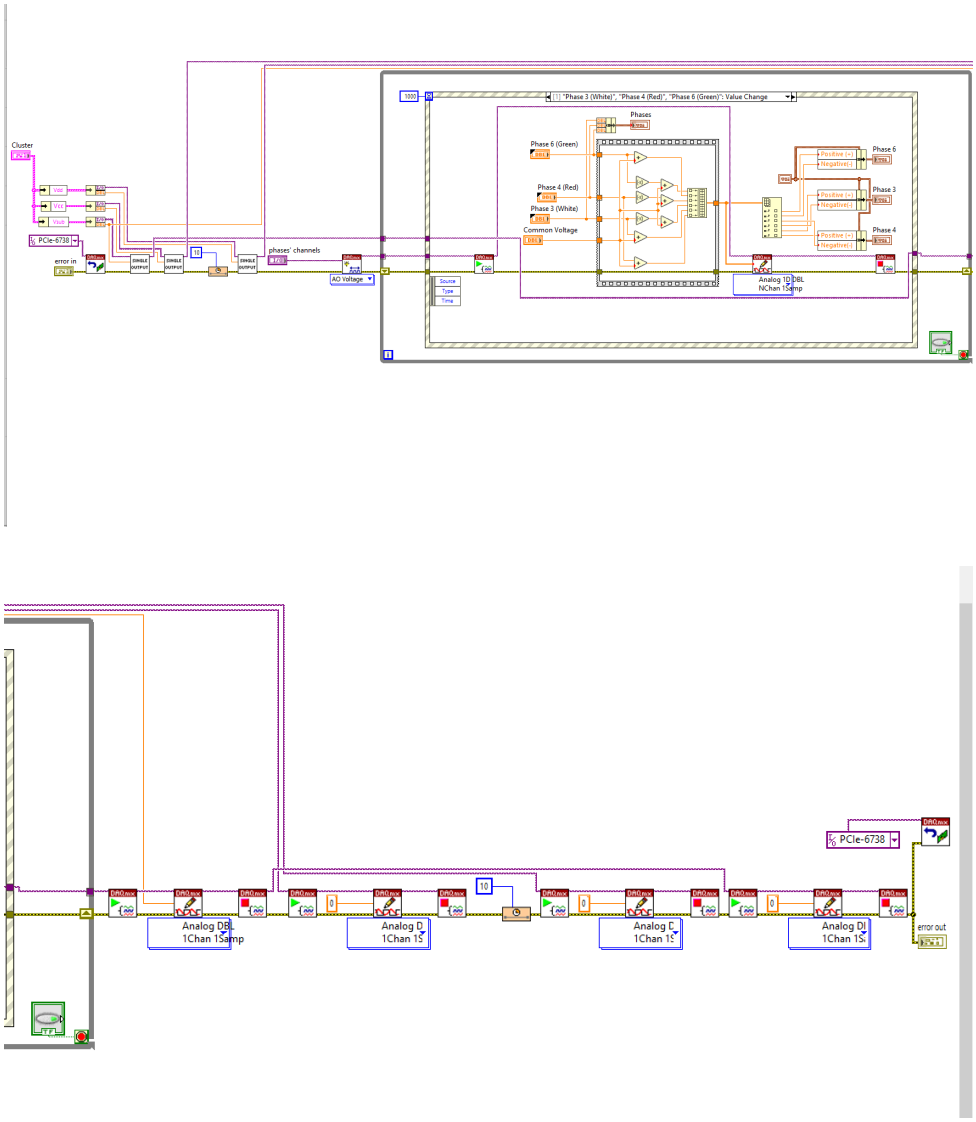

Figure 3.8: LabView Code.

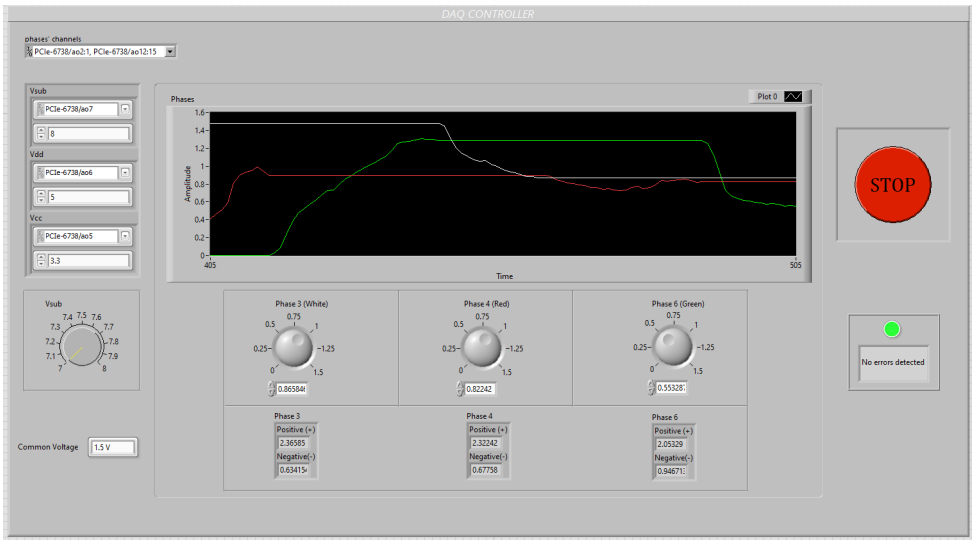

Figure 3.9: LabView front panel.

is estabilished and the output voltage of a single channel is set using the DAQmx Create Channel, DAQmx Start, DAQmx Write and DAQmx Stop blocks.
In this way, the values of Vsub, Vcc and Vdd are set in this precise order. Between the setting of Vcc and Vdd there is a time control to ensure we respect the timing schedule of the modulator.
After setting these three first voltages, the data flux enters a DAQmx Create Channel block in which the channels related to the phases' voltages are connected, then it enters in a while loop with a case event inside it.
In the case event there are three cases:
• The first one is the value change of one of the phases' voltages. In this case a vector with the six (two for each of the three phases) values is generated and wrote, using the DAQmx Start and DAQmx Write blocks, in the channels related to the phases.
The values are also given as an input to the flow chart to generate a real time graph of the phases' voltages.
• The second one is the value change of Vsub. In this case its value is updated while the phases' values remain untouched.
• The third one is the timeout which is set to one second and has the only utility of making the data flux exit the case event and the while loop when the STOP button is pushed.
After the while loop the switching off procedure starts: first of all, Vsub is set to a safe value, then Vdd is set to zero and, again respecting the time schedule of the modulator through a time control, Vcc is set to zero.
After that, Vsub is set to zero and the second DAQmx Reset block sets all the other

voltages to zero.
From the panel in Figure 3.9 it is possible to set the tension for every channel. The values for Vsub, Vdd and Vcc are set respectively to 8V, 5V and 3.3V.
The three knobs in the bottom part of the screen allow us to change the tension of the six phases we used (there are only three knobs for six phases because the phases are coupled and one is the opposite of the other) while the graph shows their real time value. The common value for the phases' voltages is set to 1.5V and the knobs range is between 0V and 1.5V since we can't have negative voltages.
The knob on the left lets us fine tune the Vsub value.
The STOP button allows us to start the switching off procedure and put all the voltages to zero safely for the modulator.
Finally, there is an error panel to monitor the correct execution of the program.

4 | Simulation and Testing

To maximize the signal-to-noise ratio and optimize the sensitivity of the realized spectrometer, preliminary simulations related to the comb generated by the AWG were performed and experimentally verified. Then, the spectrometer was assembled, and each component was meticulously tested to ensure proper functionality. All parts were mounted on a custom-made aluminum cart equipped with wheels, making the instrument portable and suitable for in field measurements.

4.1. Design and optimization of the EO-comb

The correct design of the RF signal that has to be provided by the AWG is crucial to optimize the interferogram obtained once the two combs are detected. One of the main issue of the dual comb detected signal is that there is a high-intensity peak followed by very low intensity tails where the most part of the spectroscopic information is encoded. Changing the phase relationship between comb oscillating modes allows to better uniform the signal and to increase the SNR of the measurements. The microwave signal provided by the AWG to the EOM is supposed to:

1. generate combs within 25 GHz bandwidth of the AWG;
2. set the spacing between adjacent comb modes to approximately 100 MHz, allowing for adequate sampling of the absorption features of gaseous samples at atmospheric pressures, which exhibit linewidths of about 1 GHz;
3. maintain uniform power levels for the comb modes across the entire spectral range that avoid the needs to remove the signal baseline;
4. maximize the ratio between the comb output power and the input power of the cw laser by maximizing the SSM throughput.

The last two requirements involve a trade-off regarding the maximum voltage of the AWG signal: achieving a spectrally flat comb requires driving voltage values less than or equal to V_π (which is 3 V for the modulators embedded in our SSM) to avoid nonlinear effects

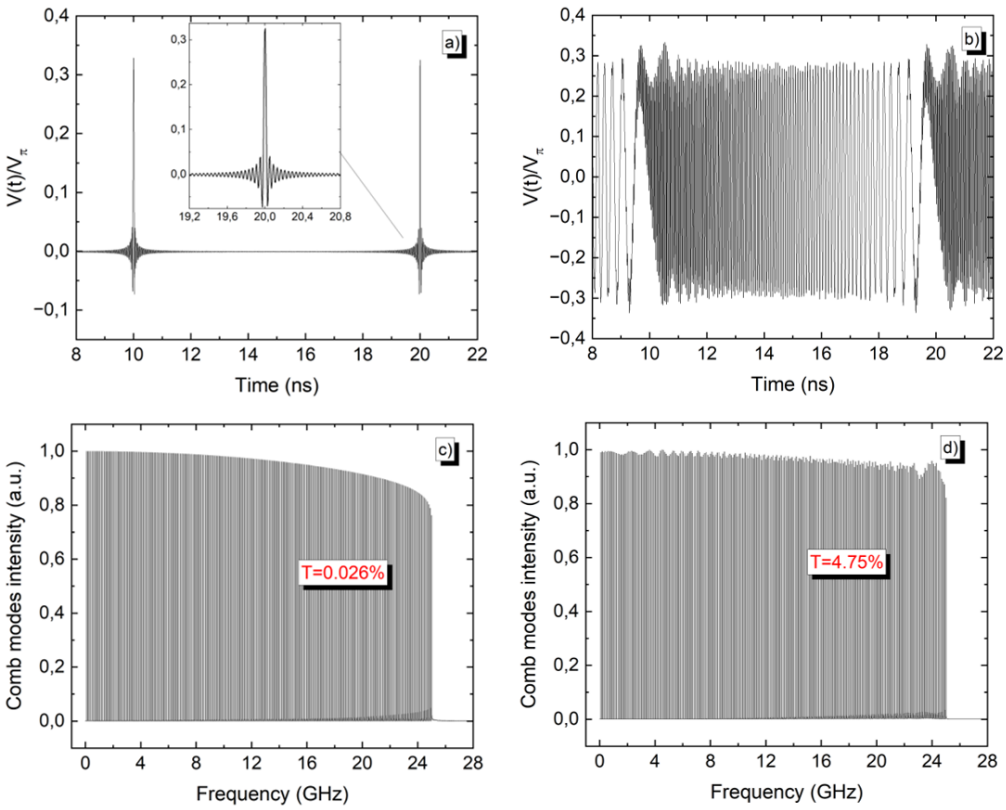

Figure 4.1: a) and b): voltage signal normalized to the peak-voltage of the modulator as a function of time, respectively for flat and parabolic spectral phase, with $f_r = 100$ MHz, 250 harmonics, peak voltage smaller than $1/3V_\pi$. c) and d): normalized distribution of the expected comb mode power, in the two cases, respectively. The absence of voltage pulses afforded by the parabolic phase allows to better exploit the transfer function of the modulator and to strongly enhance the comb mode power and the throughput T while maintaining a satisfactory spectral flatness.

and second-order sidebands, but this results in reduced comb mode power. To address this trade-off, we investigated the optimal phase values φ_m to assign to each harmonic of the microwave signal

$$V(t) = \sum_{m=0}^{N} V_0 \sin(2\pi m f_{rep} t + \varphi_m) \tag{4.1}$$

which maximize the throughput of the SSM (and thus the output comb power) by maintaining a spectral flatness at the 10% level. This study was performed by calculating the spectral response and the throughput of an intensity modulator for different phase profiles. Figure 4.1 shows the results of the simulation obtained under the operational conditions set by points 1. and 2. (250 modes spaced by 100 MHz over a 25 GHz band-

width) in two different cases: i. a flat spectral phase ($\varphi_m = 0$, left panels) and ii. an optimized parabolic phase ($\varphi_m = \pi m^2/N$, right panels). In the first case, because of the periodic rephasing of the different harmonics at the instants $t = 0, 1/f_r, 2/f_r$, ..., the driving microwave signal (panel a) is pulsed and the voltage limitation given by the AWG ($V(t) < 1/3V_\pi$) translates to a low power per comb mode and to a very low throughput (0.026 % as it can be seen in panel c). In the second case (panel b), thanks to a suitable phase profile that quenches any pulse formation, the amplitudes of the harmonics that compose the electric signal, and thus the power of the corresponding comb modes, are greatly enhanced. The throughput, in particular, increases by 2 orders of magnitude (4.75 %) and reaches a satisfactory value for applications: assuming, e.g., an optical power of 10 mW at the input of the modulator, the comb power happens to be in the 100s μW range, which is sufficient to saturate commonly used detectors.

4.2. AWG-based synthesis of a microwave dual-comb signal

In this section, we present the measured spectra generated by the AWG and we make a comparison with those simulated shown in the previous section.

To generate the spectra designed in Sec. 4.1, we firstly connected the AWG to the computer and exploiting a Matlab-based integrated tool, named iqtools, we generate combs with different spacing and different phases.

The frequency spectra of the generated signals were measured with a spectrum analyzer (Anritsu MS2830A, 3.7 GHz bandwidth), whereas the temporal profiles were measured with a 200 MHz-bandwidth digital oscilloscope (Keysight MSOX2024A).

The spectra of the generated RF frequency combs are shown in Fig. 4.2. The experimental results are in good agreement with the simulations: the comb generated by applying a parabolic spectral phase exhibits a greater average power of about -20 dBm with respect to the comb generated by setting to 0 the relative phase between the harmonics, which has an average power of about -35 dBm. Unfortunately it was not possible for us to compare the behaviour of the generated RF comb with the simulations due to the limited bandwidth of our spectrum analyzer that is 3.7 GHz. Despite this limitation, in the range covered by the analyzer the results agree with the simulations, suggesting that adding a parabolic spectral phase results into a better power stability of the higher frequencies.
We also generated combs with increasing spectral phase and a random phase, shown in Fig. 4.2(c) and in Fig. 4.2(d) respectively. Compared to the parabolic spectral phase, the

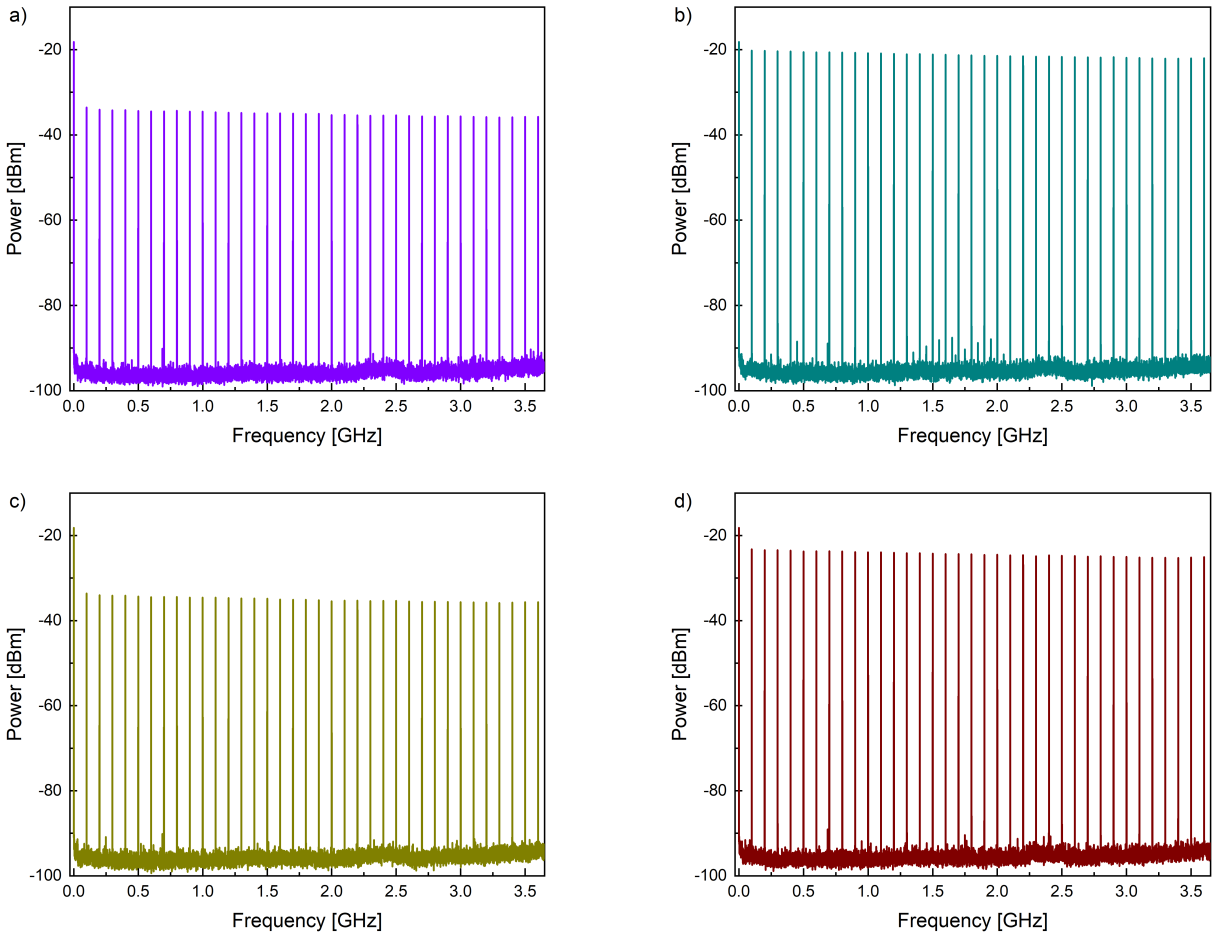

Figure 4.2: Radio frequency comb generated with different phase profiles: a) zero; b) parabolic; c) increasing; d) random.

output power seems to be significantly reduced by the sum of an increasing spectral phase, whereas it seems to be slightly reduced by imposing a random spectral phase. Moreover the random phases comb seems to have a comparable stability at higher frequency within the spectrum analyzer bandwidth. To compare with the simulation and verify the different

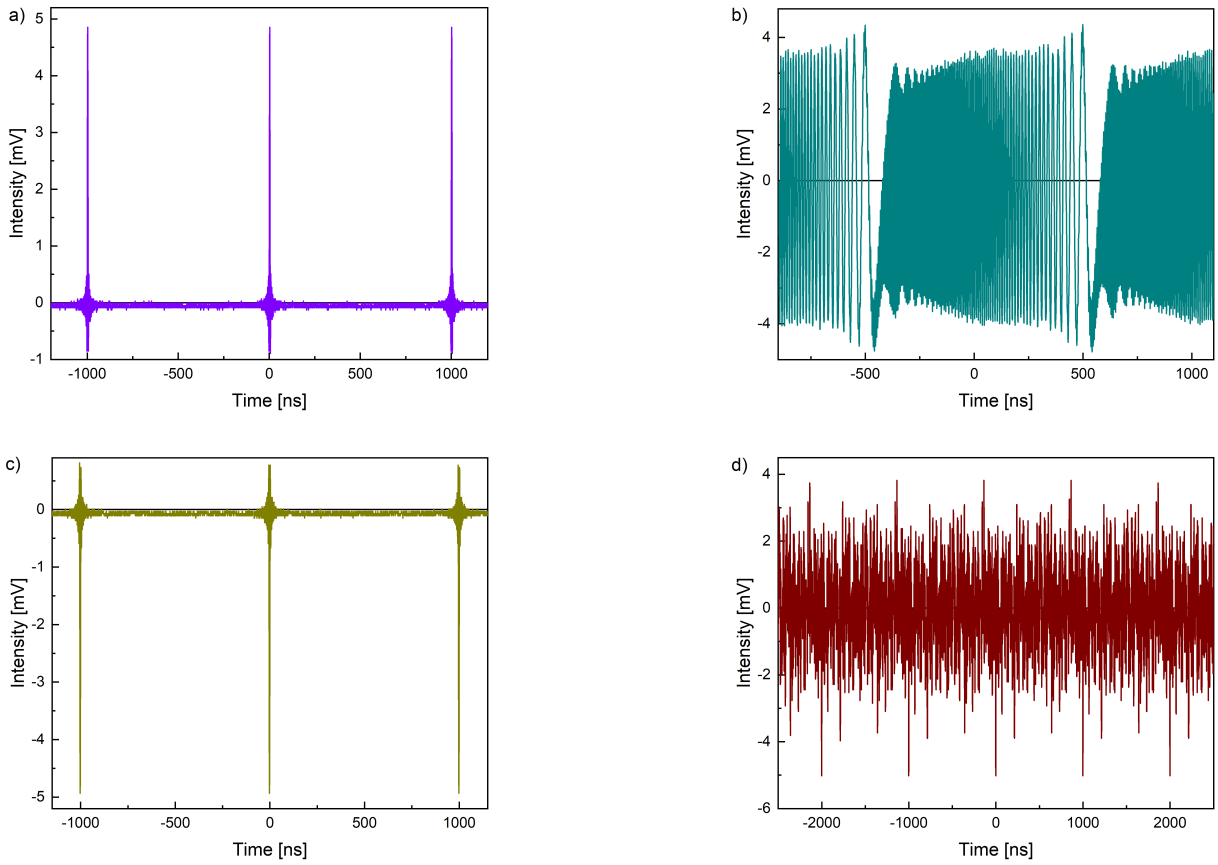

Figure 4.3: Temporal profiles of radio frequency combs generated with different phase profiles: a) Zero; b) Parabolic; c) Increasing; d) Random.

behaviour of the radio frequency comb with different phase relationship between modes we acquired their temporal profiles.

Due to the limited bandwidth of the oscilloscope (200 MHz), which cannot accommodate the wide bandwidth of the generated RF combs (around 4 GHz), the results differed significantly from the simulations, as the oscilloscope is unable to resolve the fast transients of the electric signal.

To overcome this issue, there were two possible approaches: applying a low-pass filter to the simulated signal at 200 MHz, or rescaling all the comb spacing by a factor of 50 to 500 to match the bandwidth of the generated comb to that of the oscilloscope. We then decided to perform some test with the second approach. The RF comb was generated

setting the tooth spacing at 1 MHz. Fig. 4.3 show that the measured signals now match perfectly the simulations. The fast transients of the RF comb with parabolic phase in this conditions are well resolved by the oscilloscope and the temporal duration of the peaks of the RF comb with zero phase reflects the expected duration.

After thorough analyses, we concluded that the comb generated by adding a parabolic spectral phase profile is the most suitable for our applications, providing optimal output power and stability at higher frequencies.

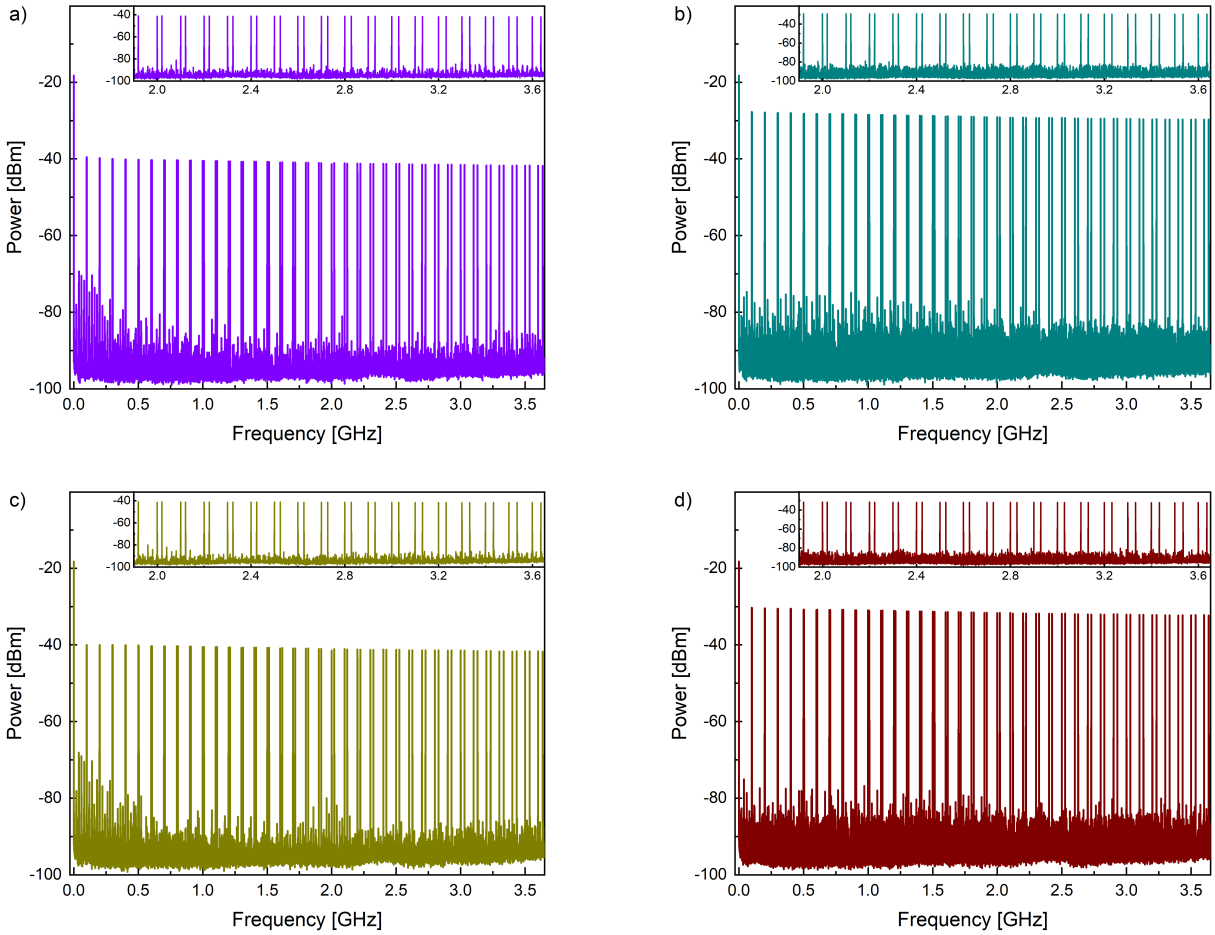

Figure 4.4: Dual combs generated with different phase profiles: a) Zero; b) Parabolic; c) Increasing; d) Random.

Working on the Matlab code we generate a radiofrequency dual comb instead of a single one: an example of a code is shown in Fig. 4.5 and the dual combs are shown in Fig. 4.4. As expected the obtained results are very similar to the result obtained for the single combs: the parabolic spectral phase addition results into greater output power and power stability. In particular, the dual comb with a parabolic spectral phase exhibits a power of

MATLAB Code Viewer

```
fs = 64e9;

tone1= 0: 100e6: 24.9e9;
tone2= 0: 100e6+100e3: 24.9e9+100e3*250;
tone3= [tone1 tone2];
tone= sort(tone3);

magnitude = zeros(1, 250);

[iqdata, ~, ~, ~, chMap] = iqtone('sampleRate', fs, 'numSamples', 0, ...
    'tone', tone, 'phase', 'Parabolic', 'normalize', 1, ...
    'magnitude', magnitude, 'correction', 0, 'channelMapping', [1 0]);

iqdownload(iqdata, fs, 'channelMapping', chMap, 'segmentNumber', 1);
```

Run Save As... Close

Figure 4.5: Matlab script for RF dual comb generation. In this example a dual comb with $f_r = 100$ MHz and with $\Delta f_r = 100$ kHz

about −28 dBm, whereas the addition of an increasing and random spectral phase leads to an output power of about −40 dBm and −30 dBm respectively. Regarding the stability at the higher frequencies, the obtained results are very similar to the single comb case, suggesting that the parabolic spectral phase addition ensures a slightly better stability, within the bandwidth of the spectrum analyzer.
We concluded therefore also for dual comb case that the parabolic spectral phase profile is clearly the most suitable in terms of output power and power stability at higher frequencies.

4.3. Development and testing of an electronic interface board driving the SSM

The spectrometer has been designed for versatile use across various fields and for performing *in situ* measurements. This is why, all the components has been mounted on a specially designed wheeled cart, providing a stable platform that minimizes vibrations. The cart is built with a modular frame easily reconfigurable and customizable. The components accommodated on the cart are:

1. Ultra-stable narrow linewidth CW laser;
2. Single side band modulator (SSM)
3. Custom designed prototypal electronic interface board

4. Temperature controller
5. Laser current drivers for the semiconductor optical amplifiers (SOA) integrated in the SSM
6. Arbitrary Waveform generator
7. Terminal block to interface the PCIe board mounted on a PC that is needed to programmatically provide the most part of the voltages needed to drive and bias the SSM
8. Personal computer with keyboard mouse and monitor to control and automatize the whole spectrometer.

The structure, composed by a cart with aluminium planes and construction rails, is divided in three levels:

- The bottom level accommodates the personal computer
- In the middle one takes place the terminal block, connected with the PCIe inside the computer, whose cables end into the breadboard, the Single Sideband Modulator connected with the breadboard trough the connector and the laser.
  Additionally, in this level are placed the current drivers for the pre and post SOA. It is worth to highlight that in this first prototypal configuration the power supplies for the operational amplifiers and for the temperature control are external. When the system is complete these last power supplies will be on this middle plane.
- The upper plane has been suitably tailored to hold the AWG but at the same time to left enough space to easily access the elements on the second plane.

The whole structure is shown in Fig. 4.6.

The majority of the design work was focused on the development of a prototype electronic board capable of interfacing the SSM with the voltage signals needed to correctly activate the SSM driver and bias the nested modulators. Before the realization, the board was designed in EAGLE. In particular, the cable layout was optimized by exploiting the optimizing functions embedded in this software. The schematic of the board is shown in Fig. 4.7. Although the dual comb setup requires driving only one of the two SSMs present in the integrated device, the board was designed to operate both modulators. Once the prototype has been thoroughly tested, the EAGLE project will enable the creation of a printed electronic board (PCB) , eliminating the need for wired connections between the components.

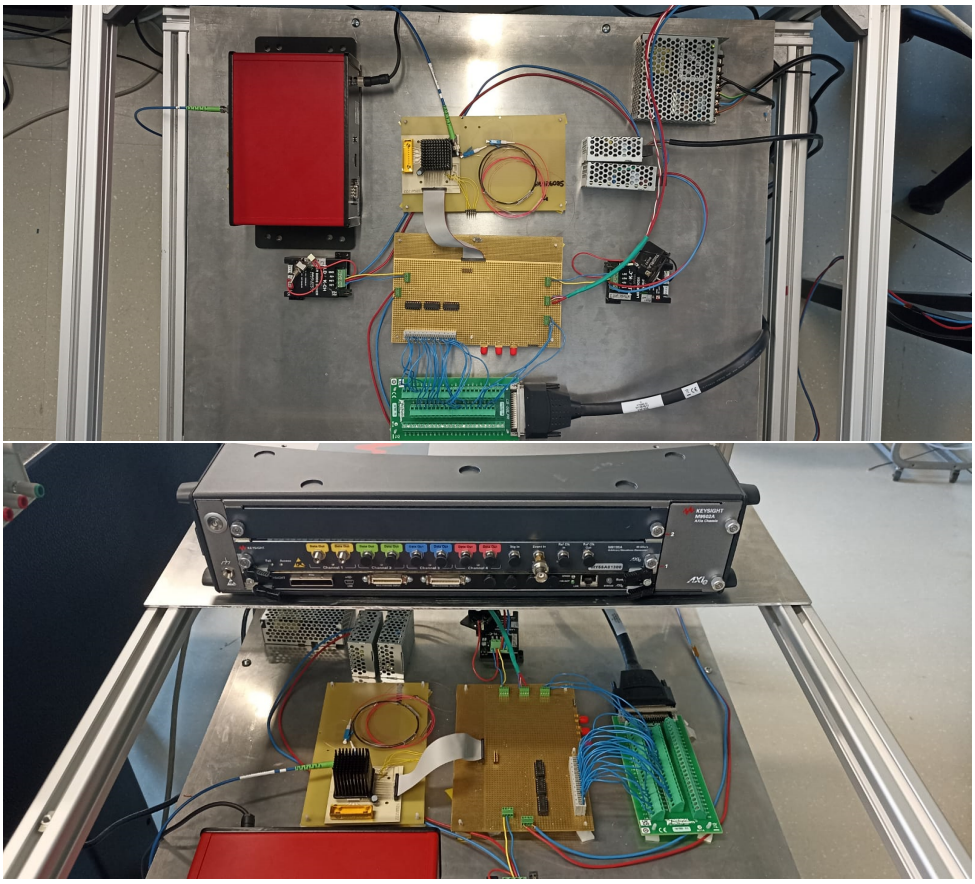

Figure 4.6: Complete set-up.

After the designing, we realize the prototype breadboard. We use a breadboard with two different pitches, since the 40 pin connector of the SSM has a very small pitch of 1.27 mm whereas all the other components have the more usual pitch of 2.54 mm. After a careful test of all connections, the breadboard was connected with the other elements of the set-up.

To check if the breadboard provides the correct voltage values at the op-amp inputs and at the terminal block with V_{cc}, V_{dd} and V_{sub}, these voltages were measured with the breadboard firstly connected to the PCIe board without the operational amplifiers.

To generate the voltage inputs we exploited the LabView script described in Ch.3.

We properly selected the channels of the PCIe by looking at the connection pinout in the datasheet of the terminal block. The connections were tested by setting the voltages to different values. For the operational amplifiers and for V_{sub} we also tested the correct functioning of the knobs present in the Front Panel of the Labview script, allowing real-time tuning of the phase voltages.

Once the connections between the DAQ board and the terminal block with V_{cc}, V_{dd} and V_{sub} properly work, we inserted the cable into the 40 pins-connector and tested the con-

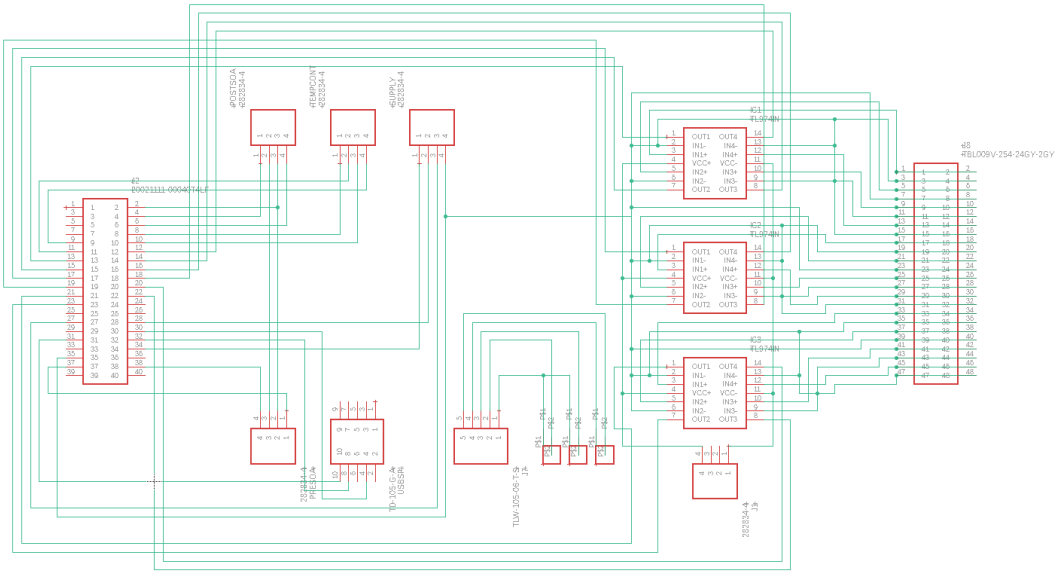

Figure 4.7: Schematic of the electronic interface

nections between the terminal block and the connector.

To guarantee the correct functioning of the device, during the modulator power-up it is fundamental providing the three voltages in a specific order: first V_{sub} and V_{cc} must be applied, then V_{dd} must be provided within 100 ms after V_{cc} application (see Fig. 4.8). The situation is similar during the modulator switching-off: V_{dd} must be first switched-off, then V_{sub} and V_{cc} with the constraint of V_{cc} switching-off within 100 ms after V_{dd}.
To better manage these timing requirements we therefore implemented a timing control on the application of V_{dd} in our LabView software. We tested this feature by acquiring by oscilloscope the three voltages in the board switching-on and in the switching-off at 0 and 10 ms delay values between the V_{cc} and V_{dd}.

An example of the measurement with the software delay set to zero is shown in Fig. 4.9(a). The voltages are provided in the correct order, and there is a delay between V_{cc} and V_{dd} of about 2 ms due to the latency time of the script.
In Fig. 4.9(b) it is shown an example of the application of the three voltages with the software delay set to 10 ms. As in the previous case, the voltages are provided in the correct order, and there are 10 additional milliseconds of delay between V_{cc} and V_{dd} as expected.
In Fig. 4.9(c) it is shown an example of the the switching off of the three voltages by setting the software delay to 0 ms: also in this case the timing is correct, with the same delay between the switching-off of V_{cc} and V_{dd} due to the latency time.
Finally, in Fig. 4.9(d) it is shown the switching-off by setting the software delay to 10

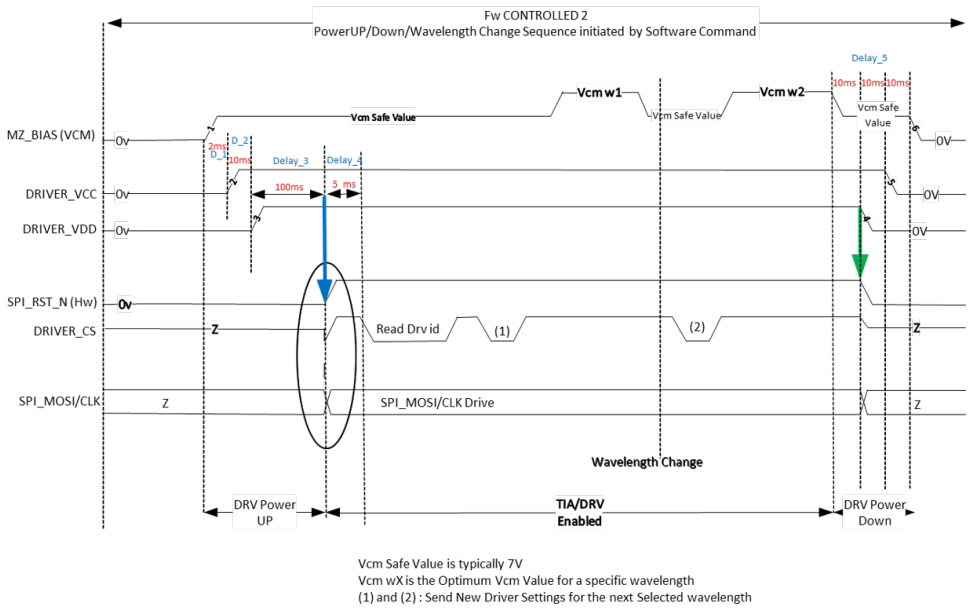

Figure 4.8: Timetable of the voltages of the modulator

ms: the timing of the switching-off is correct and 10 ms has added to the latency time between V_{cc} and V_{dd} as expected.

Testing of the phase voltages required to install the operational amplifiers. This unexpectedly proved to be one of the most challenging aspects as the op-amps initially did not respond as expected. Even without applying any voltage to the entire board, the op-amp outputs exhibited a non-zero voltage. Furthermore, when voltages were applied, they displayed unexpected behavior.
Initially, we attempted to resolve the issue by disconnecting the PCIe grounds from the board, suspecting a possible connection problem. Subsequently, we connected each operational amplifier individually and monitored its current consumption, which was significantly higher than expected under normal conditions.
Following that, we opted to test the op-amps independently from the rest of the setup. After several attempts, we discovered a configuration that proved effective: connecting the ground of the power generator to its negative output and to the V_{cc}- of the op-amp, while V_{cc}+ was connected to the positive output of the generator.
When we made the op-amps work as expected we checked the output at the end of the cable and rearranged the connections in the LabView project to have the positive and negative phases at the right pins. It was not trivial since it was not clear, when opening more than one channel at the same time, which channel corresponded to which element of the array.
The following preliminary test focused on the temperature stabilization of the chip, which

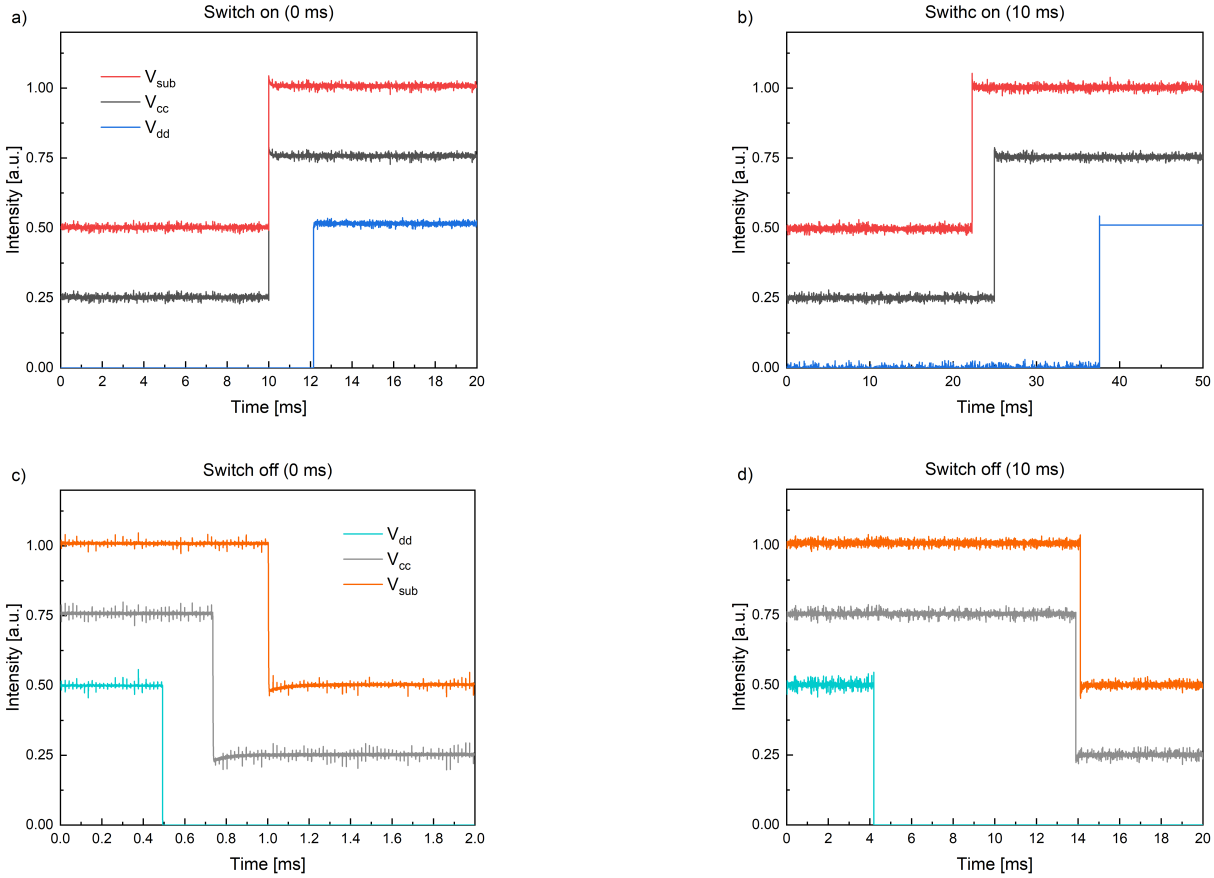

Figure 4.9: Voltages applications retards analyzed with an oscilloscope.

was maintained around 60 °C. This test demonstrated that a stability on the order of mK was achieved within 5 seconds by carefully tuning the Proportional (P) and Integral (I) parameters of the PID regulator. This level of precision ensures the chip operates within the desired thermal range, minimizing fluctuations and optimizing performance.

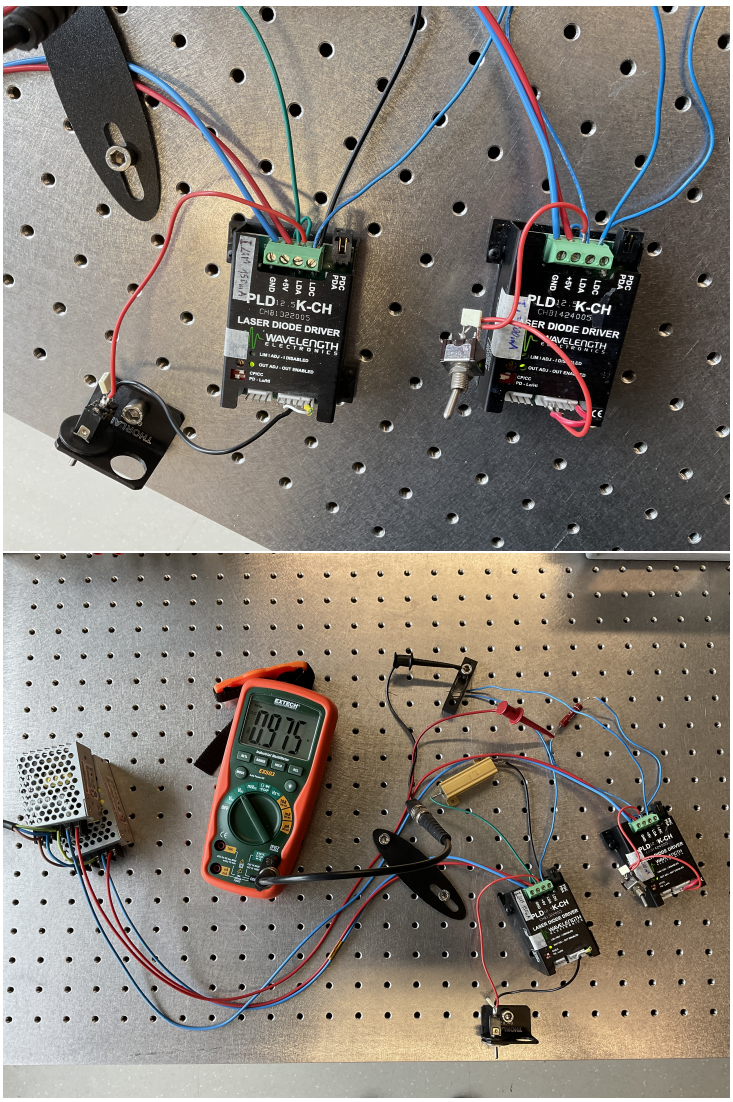

Figure 4.10: Testing of the SOA.

Additionally, the laser driver was tested in a ground cathode configuration, shown in Fig. 4.10, as required by the Semiconductor Optical Amplifier (SOA). In the datasheet of such a laser driver there were no indication about a possible cathode ground configuration, then we have to mimic this configuration to test it without the SOA. Grounding the laser cathode to the optical table, that has a separated ground with respect to the supply ground, and providing current to a dummy load we checked that the driver was able to vary the laser anode voltage to provide the current set by the trimmer. The results

confirmed that the laser driver operated correctly within this configuration, indicating that it suitable to correctly drive the SOA in the integrated device without the risk of damage.

Fig. 4.11 shows a long term power characterization of the laser, after a brief period of thermalization, measured for 2 hours using a broadband thermopile (Thorlabs S401C) with an uncertainty of ±5%.
The laser has an average power of 96.3 mW with a standard deviation of $3.91 \cdot 10^{-5}$ calculated on the last 40 minutes were the power highlights the best temperature stability. Since the laser was not in single mode emission, temperature and current were changed to find a stable, narrow single mode emission.
This ends up to be at 14.1 ℃ for the FBG, 25.2 ℃ for the chip and 720 mA current.

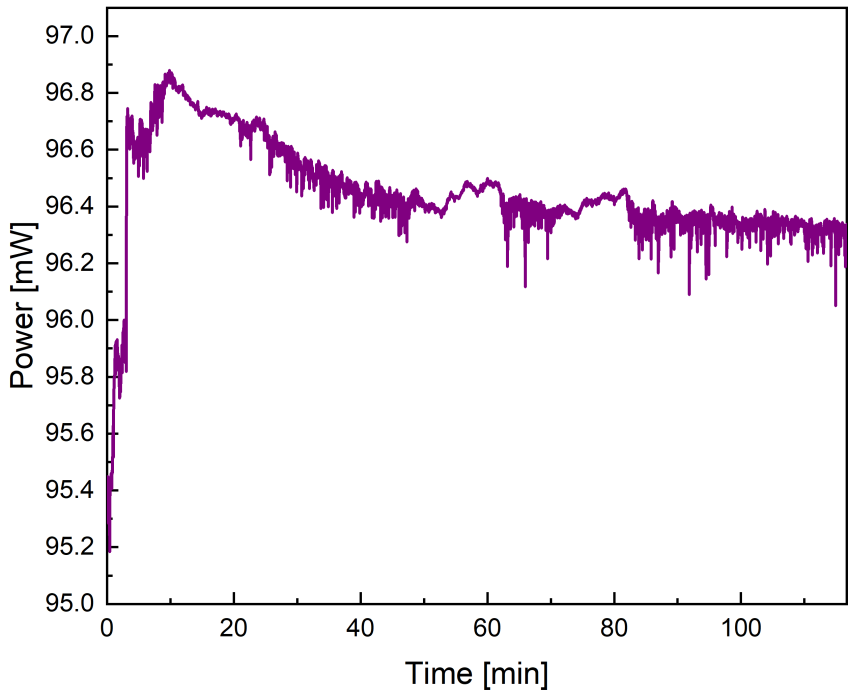

Figure 4.11: Output power of the ULN15TK laser

5 | Conclusions

In this thesis, we have reported on the extensive development of a compact and portable dual-comb spectrometer setup. This spectrometer uniquely leverages the properties of a telecom device known as a single side-band modulator (SSM), providing extreme versatility and allowing instantaneous shift between different configurations. Extensive simulations, successively confirmed by experiments, have been performed to optimize the spectrometer in terms of optical power and spectral uniformity. A prototype breadboard was designed, constructed, and rigorously tested to interface with the SSM, ensuring seamless integration and optimal performance of various components.

Additionally, significant efforts were made at the software level, involving the development and refinement of LabView code, as well as the complex process of dual comb generation using the AWG.

The results of such a multifaceted work is a fully developed dual-comb EO spectrometer that is ready for operation and testing at telecom wavelengths and in the NIR. This represents a significant advancement over traditional spectrometers based on tunable continuous-wave lasers and a simplification with respect to the usual EO spectrometers based on the combined use of intensity modulators and acousto-optical modulators.

The spectrometer is expected to offer a substantially high acquisition rate, reaching up the µs level enabling the study of fast chemical reactions. Furthermore, it promises a higher signal-to-noise ratio per spectral point and per unit of measurement time, enhancing the accuracy and efficiency of spectroscopic analyses.

The whole system has been accommodated on a mobile cart which guarantees an ease of movements and, consequentially, a wide adaptability to different measurements conditions, even for in field measurements.

The focus on the telecom wavelength range is strategically advantageous for many applications. Although it may seem limiting, it actually enables the exploitation of numerous combination or overtone vibrational bands in the near-IR. These bands are critical for detecting and quantifying a wide variety of compounds, thereby broadening the spectrometer's applicability across different fields.

Looking ahead, the potential of nonlinear optics can be harnessed to extend the dual-comb

source into the mid-IR region. Combining optical parametric oscillator with difference frequency generation it would be possible to shift the dual comb spectrometer in the mid-IR region achieving wavelengths between 3 µm and 15 µm.
This extension to the mid-IR region is expected to significantly enhance sensitivity due to the stronger fundamental rovibrational lines that lie in this so-called "fingerprint" region enabling the simultanoeus monitoring of a big amount of molecules. These advancements will open a multitude of applications, spanning from medicine to atmospheric monitoring, and are essential for studying combustion processes. The demand for a rapid acquisition rate in these fields highlights the suitability of our spectrometer for their analysis. This dual-comb EO spectrometer is expected to provide significant contributions to fields that demand precise, rapid, and sensitive spectroscopic measurements, paving the way for future innovations and applications.

Bibliography

[1] Johann Heinrich Lambert. Photometria sive de mensura et gradibus luminis, colorum et umbrae. *Klett*, 1760.

[2] August Beer. Bestimmung der absorption des rothen lichts in farbigen flussigkeiten. *Ann. Physik*, 162:78–88, 1852.

[3] Robert Resnick Robert Eisberg. Quantum physics. *John Wiley New York*, 1974.

[4] Ludwig Boltzmann. Lectures on gas theory. *Courier Corporation*, 2012.

[5] A Perrin J-M Flaud CP Rinsland LS Rothman A Goldman, RR Gamache. Hitran partition functions and weighted transitionmoments squared. *Journal of Quantitative Spectroscopy and Radiative Transfer*, 2000.

[6] Alain Campargue-Attila G Cs´asz´ar Ludovic Daumont Robert R Gamache Joseph T Hodges Daniel Lisak Olga V Naumenko Laurence S Rothman et al. Jonathan Tennyson, Peter F Bernath. Recommended isolated-line profile for representing high-resolution spectroscopic transitions (iupac technical report). *Pure and Applied Chemistry*, 2014.

[7] Orazio Svelto and David C Hanna. Principles of lasers, volume 4. *Springer*, 1998.

[8] H Friedmann A Ben-Reuven and JH Jaffe. Theory of pressure induced shifts of infrared lines. *Journal of Chemical Physics*, 1963.

[9] Yury Babikov Alain Barbe D Chris Benner Peter F Bernath Manfred Birk Luca Bizzocchi Vincent Boudon Linda R Brown et al. Laurence S Rothman, Iouli E Gordon. The hitran2012 molecular spectroscopic database. *Journal of Quantitative Spectroscopy and Radiative Transfer*, 2013.

[10] Max Born and Robert Oppenheimer. Zur quantentheorie der molekeln. *Annalen der Physik*, 1927.

[11] J Michael Hollas. Modern spectroscopy. *John Wiley and Sons*, 2004.

[12] R. Holzwarth Th. Udem, J. Reichert and T. W. H¨ansch. Accurate measurement of large optical frequency differences with a mode-locked laser. *Opt. Lett.*, 1999.

[13] R Jason Jones Steven T Cundiff Jun Ye Darren D Hudson, Kevin W Holman and David J Jones. Mode-locked fiber laser frequency controlled with an intracavity electro-optic modulator. *Optics letters*, 2005.

[14] Marco Bellini and Theodor W. Hansch. Phase-locked white-light continuum pulses: toward a universal optical frequency-comb synthesizer. *Opt. Lett.*, 2000.

[15] Ronald Holzwarth Th Udem and Theodor W H¨ansch. Optical frequency metrology. *Nature*, 2002.

[16] Jinendra K. Ranka Andrew Stentz Robert S. Windeler John L. Hall David J. Jones, Scott A. Diddams and Steven T. Cundiff. Carrier-envelope phase control of femtosecond mode-locked lasers and direct optical frequency synthesis. *Science*, 2000.

[17] AE Dunlop J Stenger DH Sutter Harald R Telle, G Steinmeyer and U Keller. Carrier-envelope offset phase control: A novel concept for absolute optical frequency measurement and ultrashort pulse generation. *Applied Physics B: Lasers and Optics*, 1999.

[18] Jun Ye Steven T Cundiff John L Hall Jinendra K Ranka Robert S Windeler Ronald Holzwarth Thomas Udem Scott A Diddams, David J Jones and TW H¨ansch. Direct link between microwave and optical frequencies with a 300 thz femtosecond laser comb. *Physical Review Letters*, 2000.

[19] C Fallnich N Haverkamp, H Hundertmark and HR Telle. Frequency stabilization of mode-locked erbium fiber lasers using pump power control. *Applied Physics B: Lasers and Optics*, 2004.

[20] Guanhao Wu Ting Hao Longzhao Lu Yang Li Rongjin Zhuang, Kai Ni and Qian Zhou. Electro-optic frequency combs: Theory, characteristics, and applications. *Laser and Photonics Reviews*, 2023.

[21] W. Zhang A. J. Metcalf F. Quinlan S. A. Diddams S. B. Papp D. R. Carlson, D. D. Hickstein. *Science*, 2018.

[22] C. Wang A. Shams-Ansari C. Reimer R. Zhu J. M. Kahn M. Loncar M. Zhang, B. Buscaino. *Nature*, 2019.

[23] B. Buscaino N. Sinclair-D. Zhu R. Cheng A. Shams Ansari L. Shao M. Zhang J. M. Kahn M. Lon˘car Y. Hu, M. Yu. *Nat. Photonics*, 2022.

[24] D.J. McCarren. *A Guide to Acousto-Optic Modulators*, 12 2007.

[25] Samir Kassi Daniele Romanini Johannes Burkart, Tommaso Sala and Marco Marangoni. Optical phase cloning by an integrated dual parallel mach–zehnder modulator. *Optics letters*, 2015.

[26] William Swann Ian Coddington, Nathan Newbury. Dual-comb spectroscopy. *Optica*, 2016.

[27] Fleisher J. Douglass K. O.-. Maxwell S. E Bielska K. Hodges J. T. Long, D. A. and D. F. Plusquellic. Multiheterodyne spectroscopy with optical frequency combs generated from a continuous-wave laser. *Optics Letters*, 2014.

[28] Vicente Duran-Hugo F. Martins Sonia Martin-Lopez Miguel Gonzalez-Herraez Miguel Soriano-Amat, Marcelo A. Soto and María R. Fernández-Ruiz. Common-path dual-comb spectroscopy using a single electro-optic modulator. *Journal of Lightwave Technology*, 2020.

List of Figures

1.1 Rovibrational energy levels as a function of the internuclear distance. Rotational levels are coloured in blue, whereas vibrational are coloured in red. 18
1.2 Rovibrational transitions between energy levels of a molecular system for the three branches P, Q and R. 21

2.1 Time domain (a) and frequency domain (b) representation of the electrical field of a laser working in mode locking regime. 24
2.2 $f-2f$ interferometer scheme. Heterodine beat note signal corresponding to f_{ceo} is obtained frequency doubling the red portion of an octave-spanning supercontinuum spectrum around ν_n and superimposing with the blue part ν_m. This signal is then compared with a reference radio-frequency signal and stabilized by a servo driving the laser pump power or an intracavity electro -optical modulator 27
2.3 Bragg construction to identify ray directions with constructive interference. 33
2.4 SSM con guration scheme. A quadrature RF signal is applied at the two branches together with appropriate bias voltages to suppress the optical carrier. The suppression of one sideband with respect to the other is achieved through the application of a 2 bias voltage at the outer interferometer. 34

2.5 (a) Simple DCS concept. Two combs with repetition rates f_r and $f_r + \Delta f_r$ are mixed and detected by a single photo-receiver. As a result of the comb structure, each pair of optical teeth yields a RF heterodyne signal at a unique RF frequency. These radio-frequencies form an RF comb of spacing Δf_r. The RF teeth can be tightly packed such that >105 comb teeth can be observed simultaneously. For much of the original DCS work, f_r was typically $\approx$ 100 MHz and Δf_r was 100 Hz to 1 kHz, but these values could vary considerably across different frequency comb sources. (b) For spectroscopy, either one or both combs are passed through the sample. The resulting absorption (or phase shifts) on the comb teeth is encoded onto the corresponding amplitude (or phase) of the measured RF comb teeth. . 37
2.6 Spectral coverage of dual-comb spectroscopy demonstrations (top band) and underlying frequency comb technologies (bottom band). 38
2.7 a) Two frequency combs (red and blue) are mixed to produce (b) the rf comb. Solid gray lines indicate filter functions applied in the rf and optical to avoid aliasing effects. (c) The equivalent time-domain picture showing the pulse-to-pulse walk-off between the two comb pulse trains. (d) The photoreceiver voltage output corresponds to the product of the two comb pulses, integrated over the receiver bandwidth. 39
2.8 Three different categories of DCS demonstrations. (a) Free-running combs can yield dual-comb spectra, but with low resolution, low frequency accuracy, and low SNR, since only limited signal averaging is possible; (b) mutually coherent combs can yield comb-tooth-resolved spectra that can be averaged for high SNR; and (c) fully referenced combs yield spectra with simultaneous high resolution, absolute frequency accuracy, and high SNR. Text boxes indicate some general rules of thumb for frequency combs based on mode-locked lasers. 43
2.9 Schematic of the multiheterodyne spectrometer. FS and FC denote fiber splitters and fiber combiners. 44

3.1 Experimental setup of the EO dual comb spectrometer 48
3.2 Laser frequency noise. 50
3.3 Laser RIN. 51
3.4 Modulator Lumentum CDM0010AC 53
3.5 Alpes Lasers TC-3 during the control of the modulator temperature. 54
3.6 WTC3293 55
3.7 Breadboard 57

3.8 LabView Code. 59
3.9 LabView front panel. 60

4.1 a) and b): voltage signal normalized to the peak-voltage of the modulator as a function of time, respectively for flat and parabolic spectral phase, with f_r = 100 MHz, 250 harmonics, peak voltage smaller than $1/3V_\pi$. c) and d): normalized distribution of the expected comb mode power, in the two cases, respectively. The absence of voltage pulses afforded by the parabolic phase allows to better exploit the transfer function of the modulator and to strongly enhance the comb mode power and the throughput T while maintaining a satisfactory spectral flatness. 64
4.2 Radio frequency comb generated with different phase profiles: a) zero; b) parabolic; c) increasing; d) random. 66
4.3 Temporal profiles of radio frequency combs generated with different phase profiles: a) Zero; b) Parabolic; c) Increasing; d) Random. 67
4.4 Dual combs generated with different phase profiles: a) Zero; b) Parabolic; c) Increasing; d) Random. 68
4.5 Matlab script for RF dual comb generation. In this example a dual comb with f_r = 100 MHz and with Δf$_r$ = 100 kHz 69
4.6 Complete set-up. 71
4.7 Schematic of the electronic interface 72
4.8 Timetable of the voltages of the modulator 73
4.9 Voltages applications retards analyzed with an oscilloscope. 74
4.10 Testing of the SOA. 75
4.11 Output power of the ULN15TK laser 76